Volume 31
DOE/DP40200-47

LLE Review

Quarterly Report

April–June 1987

Laboratory for Laser Energetics
College of Engineering and Applied Science
University of Rochester
250 East River Road
Rochester, New York 14623-1299

Volume 31
DOE/DP40200-47

LLE Review

Quarterly Report

Editor: W. Donaldson
(716) 275-5347

April–June 1987

Laboratory for Laser Energetics
College of Engineering and Applied Science
University of Rochester
250 East River Road
Rochester, New York 14623-1299

This report was prepared as an account of work conducted by the Laboratory for Laser Energetics and sponsored by Empire State Electric Energy Research Corporation, General Electric Company, New York State Energy Research and Development Authority, Ontario Hydro, the University of Rochester, the U.S. Department of Energy, and other United States government agencies.

IN BRIEF

This volume of the LLE Review, covering the period April–June 1987, contains a summary of the recent high-density campaign on the OMEGA laser system; a report on the absorption and radiation of energy from spherically irradiated targets; and a computer model describing the source of hot spots in the OMEGA laser. The section on advanced technology has reports on a method for accurately measuring the phase of a high-power laser and the development of an extremely bright and compact laser. Finally, the activities of the National Laser Users Facility and the GDL and OMEGA laser facilities are summarized.

The highlights of this issue are

- The high-density campaign using gas-filled targets on the OMEGA laser system resulted in fuel compressions of 50 times liquid DT density.
- Measurements on spherically irradiated targets have demonstrated that the one-dimensional hydrodynamic code *LILAC* can accurately predict the absorption of ultraviolet radiation and the subsequent production of x rays.
- The source of hot spots in the target-plane intensity profile of the OMEGA ultraviolet beams has been identified. Small aberrations in the infrared phase profile cause the third-harmonic light to fragment into several small beamlets in the target plane.
- A method has been developed to accurately measure the phase of a high-power laser beam. Variations as small as $\lambda/50$ can be

measured, making it possible to identify source of the hot spots in the OMEGA laser beam.

- An extremely bright and compact laser has been developed. This laser, which fits on a tabletop, has achieved 0.5 J in 1.0 ps and can attain a brightness of 4×10^{18} W/cm^2 $\Delta\Omega$ when focused with an $f/1$ lens.
- A cryogenic target positioner was installed and activated on the OMEGA target chamber. The first in a series of shots was taken to achieve high-density implosions of cryogenic targets.

CONTENTS

Stephen Swales (left) and Nitin Sampat, members of the Optical Engineering Group, conduct research and development activities involving scientific image processing and software development for use in wave-front analysis of the OMEGA laser beams.

Section 1
PROGRESS IN LASER FUSION

1.A A Summary of Recent High-Density Experiments on OMEGA

During the first five months of 1987, experiments on OMEGA have concentrated on creating measurable high-density laser-fusion compressions in gas-filled spherical targets. To this end, experimental and theoretical programs have been conducted to address issues key to the successful implosion of ablatively driven, low-aspect-ratio targets. These programs have centered on (a) the characterization of the current level of target illumination uniformity with the up-converted 24 beams of OMEGA; and (b) the performance of a number of scaling experiments on solid and shell targets to correlate experiments with theoretical predictions and determine sensitivity of specific targets to illumination uniformity. These studies have resulted in the characterization of glass shell and low-Z ablator shell target implosions that have demonstrated final compressed fuel densities of ~ 50 times liquid density (XLD), with absorbed laser energies of < 1 kJ. This report describes the most important features and results of these experiments.

Two basic target designs were examined. The first was a glass shell with wall thickness $(\Delta R)_o \sim$ (3–6 μm) and a radius of $(R_o) \sim 100\,\mu$m or $150\,\mu$m, filled with D_2 or DT to pressures of 10–100 atm.[1] This type of target is predicted to have a relatively modest in-flight aspect ratio $(R/\Delta R)$ and should stagnate with a wide range of convergence ratios (R_o/R_t), where R_t is the final core radius, depending on gas pressure and shell thickness. It is a good target design to examine potential degradation of target performance due to illumination

nonuniformities. The second target design had similar overall size and fuel conditions, but had a target wall of a 3-μm glass pusher, overcoated with various thicknesses of parylene.[2] The addition of a low-Z ablator should reduce the level of radiational fuel preheat, and produce, depending on ablator thickness, a colder (lower isentrope) implosion leading to higher fuel densities.

These targets were irradiated with up to 1.5 kJ of 351-nm laser light from the 24-beam OMEGA facility,[3] in pulses of $\sim$700-ps duration. Estimates of the overall illumination intensity distribution were made from detailed beam-footprint characterization of each of the OMEGA beams. This was done by two independent methods: UV photography of an equivalent target plane (described in the article entitled "High-Power Laser Interferometry" in this issue), and x-ray photography of individual beams focused on solid, spherical high-Z (Au or Cu) targets.[4] The overall level of uniformity, determined from spherical mode decomposition of the intensity distribution, was $\sim$20%; however, this included some microscopic hot-spot structure ($\sim$20-μm scale size) having intensities up to three times the nominal intensity. The hot-spot structure has been determined to arise from the integral effects of wave-front nonuniformities imprinted on the beam distribution during propagation through the laser amplifier chain.[5]

A comprehensive set of plasma, x-ray, and nuclear diagnostics was deployed to characterize these implosions, to compare with the predictions of one-dimensional (1-D) and two-dimensional (2-D) hydrodynamic code calculations. Emphasis in these experiments was placed on those diagnostics that provided information on the compressed fuel conditions.[6] The principal diagnostics were neutron dosimetry, neutron time-of-flight spectrometry,[7] shell areal density measurements by neutron activation,[8] x-ray microscopy,[9] and time-resolved x-ray photography.[10] In addition, some estimates of the fuel areal density were obtained from measurements of the secondary-reaction products of D_2-filled targets.[11,12]

Characterization of the laser energy coupling to the target, and its partition to x rays, was in good agreement with the predictions of the 1-D hydrodynamic code *LILAC*, assuming modest (f = 0.06) thermal flux inhibition.[13] The details of the data on absorption and x-ray calorimetry are described in the article entitled "Absorption and Radiation of Energy from Spherically Irradiated Targets" in this issue. The results support the model assumption of predominant inverse-bremsstrahlung absorption, with very low levels ($\sim 10^{-3}$) of superthermal electron generation. Good agreement between measured and predicted values of the absorption for the low-Z ablator targets was also obtained. Reliable x-ray measurements were not obtained for these targets.

X-ray photographic measurements of the glass shell correlated well with *LILAC* predictions of the shell conditions and flight during the implosion. Figure 31.1 provides an illustration of this. Figure 31.1(a) shows a ($\sim$2-keV) x-ray microscope image of a glass shell target and its azimuthally averaged line profile with target radius. The x-ray emission from the outer regions of the image, resulting from the hot,

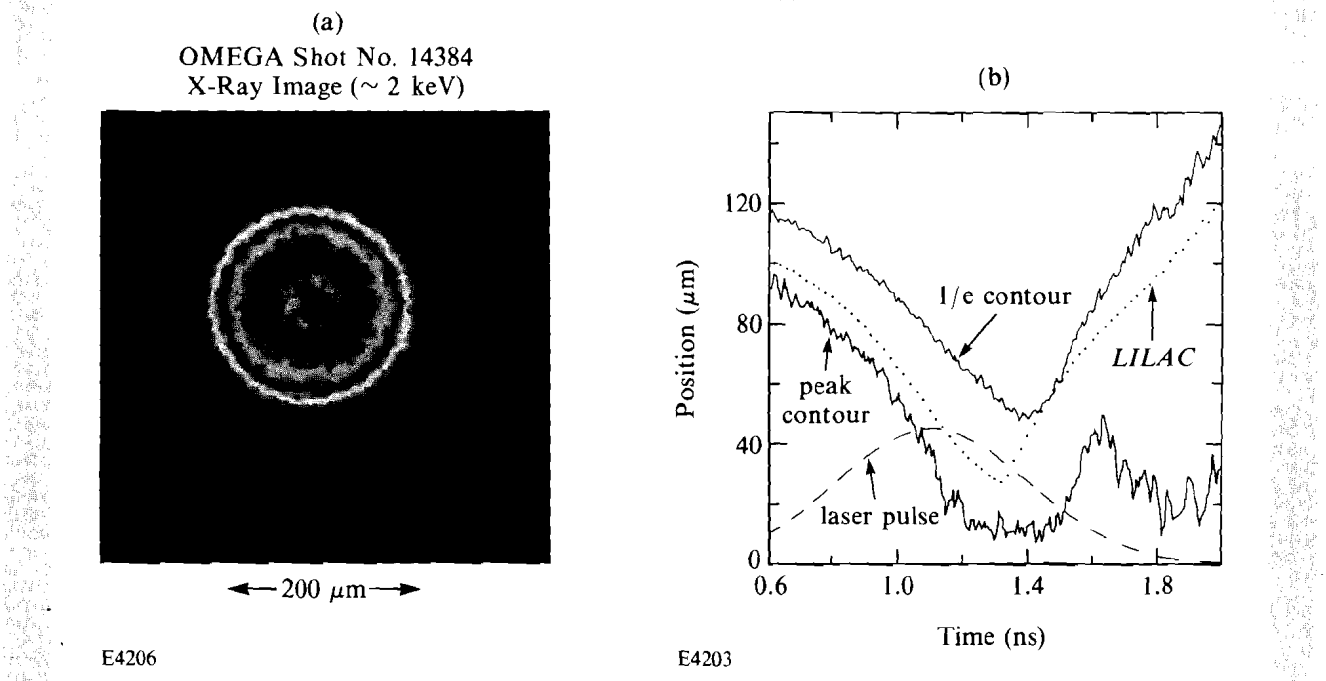

Fig. 31.1
Detailed x-ray photography of an imploding glass shell target. (a) Details of an x-ray microscope image and (b) reduced R-T distribution of x-ray emission acquired with a streak x-ray pinhole camera.

high-density region of the shell during its acceleration, is well modeled by *LILAC*. These measurements support the view that this phase of the implosion is symmetric; the measurements are substantiated by time-correlated[10] x-ray streak photography of the emission. The trajectory of the emission, deduced from digitized streak data, agrees well with 1-D hydrodynamic code predictions,[14] as demonstrated in Fig. 31.1(b). Moreover, there is indirect evidence for integral stagnation of the shell in that a radial minimum exists in the x-ray emission throughout the implosion. However, details of the fuel shell interface are not produced by this diagnostic. It therefore cannot determine the extent, if any, of pollution of the fuel by cold fragments from the inner shell.

This behavior appears to be more complex with the low-Z ablator targets. With these targets, there is evidence, both from time-resolved x-ray imaging[14] and time-resolved x-ray line spectroscopy on special signature layer targets,[15] of anomalous early lightup of inner regions of the shell. This phenomenum is most probably associated with intense hot spots in the beam distribution. Its effect on the inner fuel region and the final implosion is not fully understood at this time and is under investigation.

The measured neutron yield for glass shell targets is close to the 1-D hydrodynamic code predictions for low-convergence-ratio targets, as in Fig. 31.2. Since the neutron yield is a sensitive function of the fuel temperature, this approximate agreement indicates that targets that stagnate to fairly large core sizes ($\gtrsim$ 30 μm) maintain good symmetry throughout the implosion. However, Fig. 31.2 shows that as the expected convergence ratio of the target increases, the measured

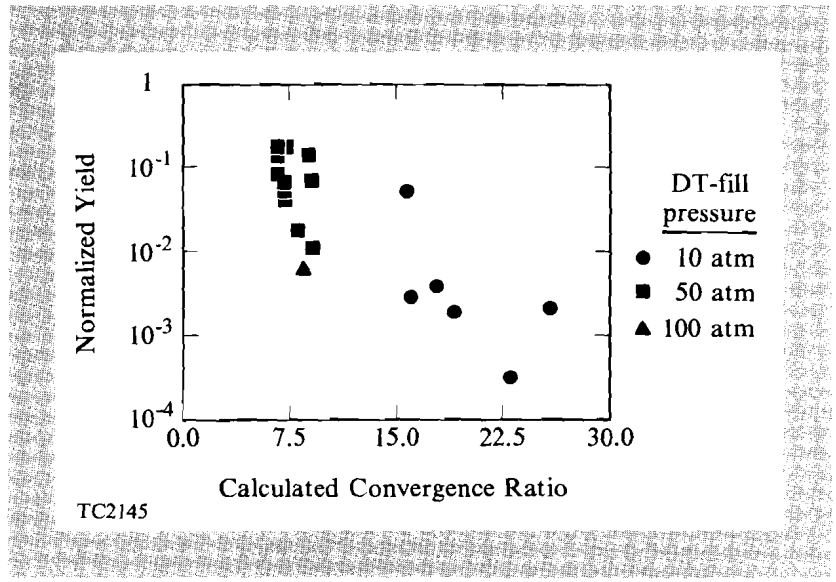

Fig. 31.2
Dependence of the ratio of the measured-to-predicted neutron yield as a function of the calculated convergence ratio.

neutron yield is severely degraded. A similar, in fact steeper, dependence was observed in earlier experiments with large-aspect-ratio targets.[16] This feature is most probably dependent on the illumination uniformity. The improved level of uniformity in the latest results lessens the falloff toward higher convergence ratios.

The most reliable scaling data from which the compressed core density can be inferred was collected from neutron activation of silicon in the glass. The details of this diagnostic system on OMEGA have been described previously.[6] However, for the present series of experiments a modification was made to the target debris collection system used to capture a fraction of the imploded shell, which has been activated by the neutron burst. In all previous experiments,[17] the debris collection cone had an efficiency of $\sim 1\%$, limited by beam geometrical considerations. However, for the present experiments, this cone collector was augmented with a plasma blowoff shroud, produced off the inside of a metal enclosure, through which the beams are focused onto the target (Fig. 31.3). For these glass shell targets, the overall collection efficiency was measured to be 25%. This efficiency level permitted the measurement of Y_n $<\rho\Delta R>$ values as low as 4×10^5. The variation of shell $\rho\Delta R$ as a function of calculated convergence ratio is shown in Fig. 31.4(a). Both experimental data and 1-D code predictions are shown. As expected, the compressed shell $\rho\Delta R$ increases with the calculated convergence ratio. The experimental data follows the code predictions quite well, at least to convergence ratios of ~ 20. Above this value, there is a falloff in the experimental data. This falloff can also be seen by comparing the measured to the predicted value of $\rho\Delta R$ [Fig. 31.4(b)]. Similar data for low-Z ablator targets is shown in Figs. 31.4(c) and 31.4(d). The degradation in target performance is even more marked in this case.

From a knowledge of the measured shell $\rho\Delta R$, and with the assumptions of implosion symmetry, isotropic fuel density, and negligible fuel-shell mixing, it is possible to estimate the fuel density at peak neutron yield.[18] With these assumptions it is easy to show that

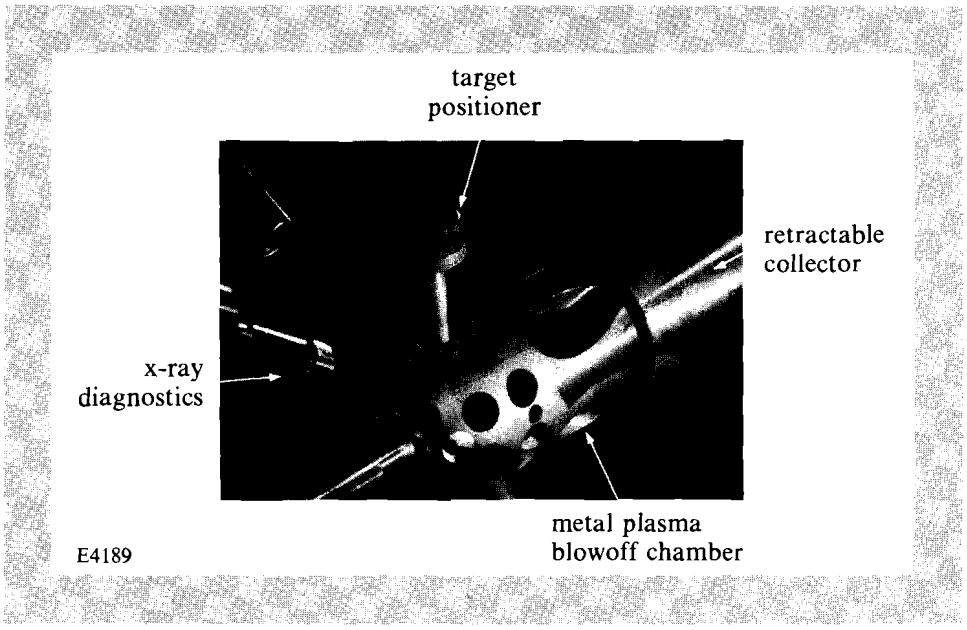

Fig. 31.3
Photograph of the plasma shroud enclosure used to boost the debris-collection efficiency.

$$\left(\frac{\rho_f}{\rho_{fo}}\right)^{2/3} = \frac{\rho\Delta R}{\rho_o \Delta R_o}\left[1+\frac{\Delta R}{R_f}+\frac{1}{3}\left(\frac{\Delta R}{R_f}\right)^2\right]\Big/\left[1+\frac{\Delta R_o}{R_{fo}}+\frac{1}{3}\left(\frac{\Delta R_o}{R_{fo}}\right)^2\right], \quad (1)$$

where ρ_f and R_f are the fuel density and radius, ρ and ΔR are the pusher density and radius, and the suffix o represents the original, unimploded value. For the thick-walled targets considered here, it can be shown that a target having fuel mass M_f and pusher mass M_p, the compressed fuel density can be expressed as

$$\rho_f = \left\{2\left(\frac{3M_f}{4\pi}\right)^{\frac{1}{3}}\left[\left(1+\frac{M_p}{2M_f}\right)^{\frac{1}{3}}-1\right]\right\}^{-\frac{3}{2}}(\rho\Delta R)^{\frac{3}{2}}. \quad (2)$$

For the data shown in Fig. 31.4, the corresponding densities are shown in Fig. 31.5. The estimated fuel density can exceed 50 XLD (10 g/cc) for both glass shell and low-Z ablator targets.

In summary, these experiments have demonstrated the achievement of high compressed fuel densities – in excess of 50 XLD, in targets irradiated by the 351-nm OMEGA laser system – for exceedingly modest incident laser energies (< 1.5 kJ). These implosions, to first order, agree well with the predictions of *LILAC*, at least for expected convergence ratios of <20. The influence of nonuniformities in the irradiation distribution is assessed from the degradation in the neutron yield with the convergence ratio. The impact of hot spots in the beam distribution on low-Z ablator targets is evidenced by early x-ray lightup times in the shell and by lower than predicted yields. This phenomena in CH targets is under further study, since most high-gain ignition demonstration targets are fabricated of polymer materials. Nonetheless, the close agreement of the measured and predicted shell areal densities for both glass and low-Z ablator targets is encouraging and augurs well for our upcoming cryogenic target implosions, which should produce much higher compressed fuel densities. Progressive

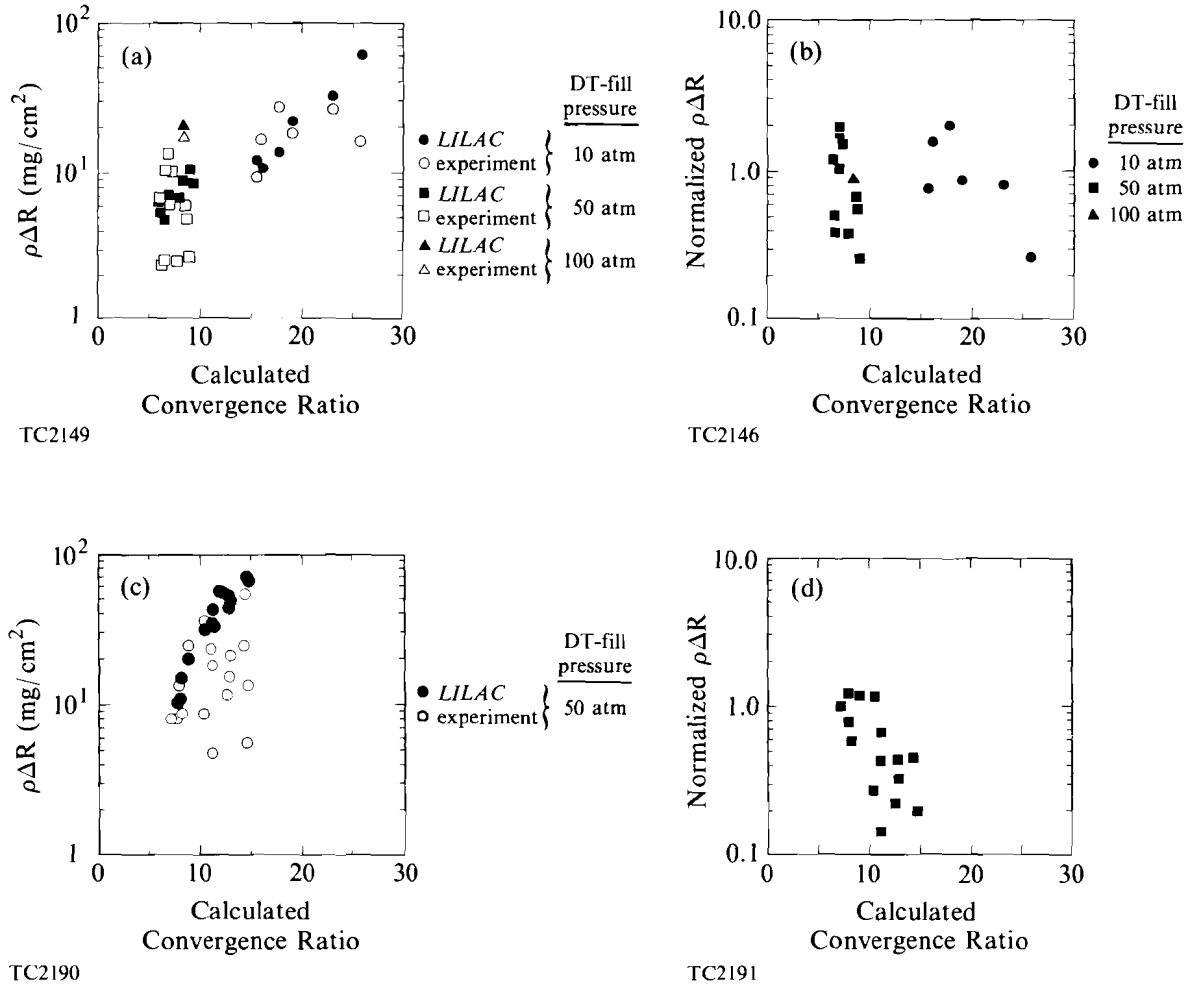

Fig. 31.4
Summary of shell areal density data acquired on glass shell targets (a) and (b) and on low-Z plastic ablator targets (c) and (d).

improvement of the illumination uniformity, and elimination of the effects of hot spots in the intensity distribution, should permit the symmetric implosion of targets having convergence ratios as high as those required for ignition scaling experiments.

ACKNOWLEDGMENT

This work was supported by the U.S. Department of Energy Office of Inertial Fusion under agreement No. DE-FC08-85DP40200, and by the Laser Fusion Feasibility Project at the Laboratory for Laser Energetics, which has the following sponsors: Empire State Electric Energy Research Corporation, General Electric Company, New York State Energy Research and Development Authority, Ontario Hydro, and the University of Rochester. Such support does not imply endorsement of the content by any of the above parties.

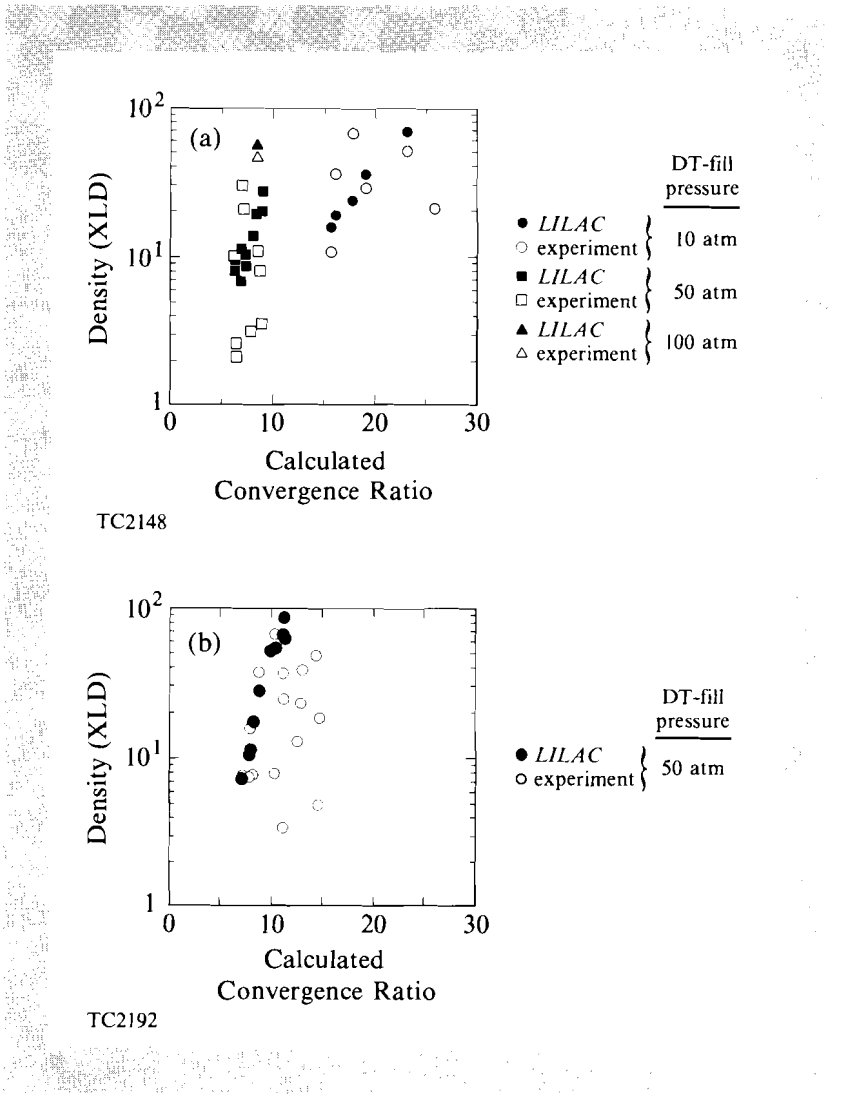

Fig. 31.5
Estimated fuel densities for glass shell and low-Z ablator targets.

REFERENCES

1. Fabrication and DT filling of the glass shells used in these experiments were performed by KMS Fusion, Inc., Ann Arbor, Michigan.

2. These targets were fabricated by the LLE target fabrication group. Polymer overcoats were applied by the bounce-coating technique [R. Q. Gram, H. Kim, J. F. Mason, and M. Wittman, *J. Vac. Sci. Technol. A* **4**, 1145 (1986)]. All targets were supported on micron-size silk fibers.

3. J. M. Soures, R. J. Hutchison, S. D. Jacobs, L. D. Lund, R. L. McCrory, and M. C. Richardson, in the *Proceedings of the Tenth Symposium on Fusion Engineering*, Philadelphia, PA (1983), p. 1392.

4. F. J. Marshall, P. A. Jaanimagi, M. C. Richardson, C. Rapp, S. Morse, R. Hutchison, S. Noyes, T. Kessler, and W. Seka, presented at the 17th Anomalous Absorption Conference, Tahoe City, CA, 17–22 May 1987.

5. T. Kessler, S. Skupsky, W. Seka, L. Feinberg, S. Jacobs, K. Marshall, N. Sampat, D. J. Smith, and S. Swales, *Proc. of the 1987 Conf. on Laser and Electro-Optics* (CLEO '86), Baltimore, MD (IEEE, New York; OSA, Washington, DC, 1987), p. 36.

6. M. C. Richardson, R. F. Keck, S. A. Letzring, R. L. McCrory, P. W. McKenty, D. M. Roback, J. M. Soures, C. P. Verdon, S. M. Lane, and S. G. Prussin, *Rev. Sci. Instrum.* **57**, 1737 (1986).

7. S. A. Letzring, G. Pien, L. M. Goldman, M. C. Richardson, and J. M. Soures, *Rev. Am. Phys. Soc.* **30**, 1481 (1985).

8. E. M. Campbell, W. M. Ploeger, P. H. Lee, and S. M. Land, *Appl. Phys. Lett.* **36**, 965 (1980).

9. M. C. Richardson, G. G. Gregory, R. L. Keck, S. A. Letzring, R. S. Marjoribanks, F. J. Marshall, G. Pien, J. S. Wark, B. Yaakobi, P. D. Goldstone, A. Hauer, G. S. Stradling, F. Ameduri, B. L. Henke, and P. A. Jaanimagi, in *Laser Interaction and Related Plasma Phenomena.*, edited by H. Hora and G. H. Miley (Plenum Press, New York, 1986), Vol. 7, p. 179.

10. G. G. Gregory, S. A. Letzring, M. C. Richardson, and C. D. Kiikka, *High Speed Photography, Videography, and Photonics III* (SPIE, Bellingham, WA, 1985), Vol. 569, p. 14.

11. E. G. Gamalii, S. Yu. Gus'kov, O. N. Krokhin, and V. B. Rozanov, *JETP Lett.* **21**, 70 (1975).

12. H. Azechi *et al.*, *Appl. Phys. Lett.* **49**, 555 (1986).

13. R. C. Malone, R. L. McCrory, and R. L. Morse, *Phys. Rev. Lett.* **34**, 721 (1975).

14. P. A. Jaanimagi, G. G. Gregory, D. K. Bradley, J. Delettrez, F. J. Marshall, P. W. McKenty, M. C. Richardson, and C. P. Verdon, presented at the 17th Annual Anomalous Absorption Conference, Tahoe City, CA, May 1987.

15. D. K. Bradley, P. Audebert, J. Delettrez, R. Epstein, G. G. Gregory, B. L. Henke, P. A. Jaanimagi, M. C. Richardson, and B. Yaakobi, presented at 17th Annual Anomalous Absorption Conference, Tahoe City, CA, May 1987.

16. M. C. Richardson, P. W. McKenty, F. J. Marshall, C. P. Verdon, J. M. Soures, R. L. McCrory, O. Barnouin, R. S. Craxton, J. Delettrez, R. L. Hutchison, P. A. Jaanimagi, R. Keck, T. Kessler, H. Kim, S. A. Letzring, D. M. Roback, W. Seka, S. Skupsky, B. Yaakobi, S. M. Lane, and S. Prussin, *Laser Interaction and Related Plasma Phenomena*, edited by H. Hora and G. H. Miley (Plenum Press, New York, 1986), Vol. 7, p. 421.

17. M. C. Richardson, P. W. McKenty, R. L. Keck, F. J. Marshall, D. M. Roback, C. P. Verdon, R. L. McCrory, J. M. Soures, and S. M. Lane, *Phys. Rev. Lett.* **56**, 2048 (1986).

18. Lawrence Livermore National Laboratory Report UCRL-50021-79, p. 6-60.

1.B Absorption and Radiation of Energy from Spherically Irradiated Targets

The coupling of high-power lasers to solid matter is important to direct-drive laser fusion. Single-beam experiments at 1054 nm, 526 nm, 351 nm, and 266 nm on planar targets have shown higher absorption and lower numbers of fast electrons for shorter-wavelength laser irradiation.[1-3] It is important to determine how uniformly irradiated spherical targets couple incident laser energy. Absorption of 526-nm laser radiation, in the intensity range of 10^{14}–10^{16} W/cm^2, has been measured for spherical targets.[4] This work is a continuation of previously reported six-beam irradiation of spherical targets at 351 nm.[5] The absorption of 24 351-nm laser beams by spherical targets was measured.

This study used the 24 UV beams of the OMEGA Nd:phosphate-glass laser facility, which have been up-converted to a wavelength of 351 nm. The laser energy is focused onto spherical targets with 60-cm focal-length lenses (*f*/3) with a lateral pointing accuracy of 10 μm and an axial pointing accuracy of 50 μm. The intensity levels of the 24 beams were balanced to within 6% of each other. Tangential focus of Gaussian spatial profile beams at the energy balance stated above yield an overall variation in intensity of 20% for a 300-μm-diameter target.

The absorbed energy and x-ray radiation were determined for solid glass spheres with diameters between 90 μm and 800 μm. The laser energy was between 1.0 kJ and 1.5 kJ, with a 700-ps to 800-ps pulse width. The range of laser intensity resulting from the above conditions was 5×10^{13} to 5×10^{15} W/cm^2. All 24 beams were focused eight target radii beyond target center; marginal rays were thus tangent to the target surface. The absorbed energy was measured with a set of 15 differential plasma calorimeters symmetrically placed around the target chamber. The energy radiated into x rays was determined by a single, differential x-ray calorimeter with a solid angle of 0.26 mstr. The measured absorbed energy to laser energy and radiated energy to absorbed energy are plotted in Fig. 31.6. The absorbed energy fraction shows a larger variation over the intensity range than does the radiated energy fraction.

The scaling of absorbed energy with incident laser energy is shown in Fig. 31.7(a). The solid lines show the absorption for the experimental irradiation conditions predicted by the 1-D hydrodynamic code *LILAC*. The assumed phenomenological flux-limit parameter is $f = 0.06$. The component of absorption due to inverse bremsstrahlung is calculated using a self-consistent ray-tracing model. The beams are incident at tangential focus, as in the experiment, and the rays are traced through the 1-D refractive-index distribution, using the assumptions of geometrical optics. An additional component of absorption is included at the turning point of the ray. This small fraction ($\sim$ 15%) is included to simulate resonance absorption. Calculations omitting this additional energy are consistent with the data

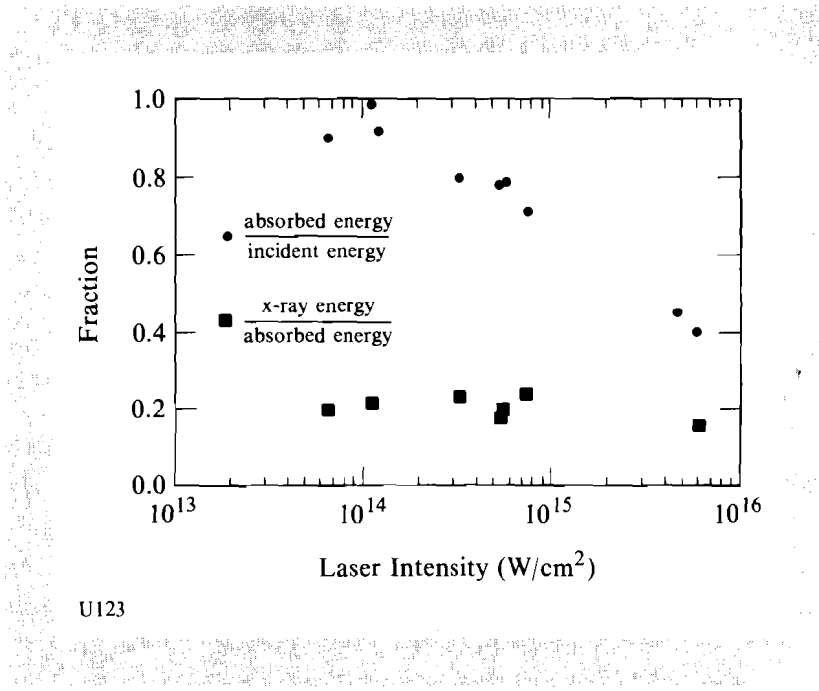

Fig. 31.6
Energy absorption versus laser intensity and radiation fraction versus laser intensity.

in the low- to mid-intensity range, but predict less absorption than is observed at intensities above 10^{15} W/cm^2. It should be noted that some resonant absorption and/or parametric decay instability occurs at 351 nm, but the energy coupled to the electrons is too low to be observed from the x-ray spectrum or to present a significant preheat problem.

Tangential-focus conditions were used in the experiment to provide good irradiation uniformity and optimum coupling of energy to the target. The solid lines in Fig. 31.7(a) show the calculation predictions for four different focusing conditions. These calculations were done for the OMEGA beam profile and for focal positions ranging from six to 12 target radii beyond the center of the target. Figure 31.7(b) shows the dependence of the absorbed-energy fraction on laser focus. The solid line is the *LILAC* prediction for an incident laser intensity of 10^{14} W/cm^2. The experimental points were measured with the same incident-laser intensity and for a laser focus range from four to eight target radii from the target center.

Because of the energy constraints, the higher illumination intensities are attained by using smaller-diameter targets. This gives rise to shorter coronal-density scale lengths and higher refractive losses. The net effect is to reduce the measured absorption. Previously reported planar target data indicate higher values of absorbed energy for intensities above mid-10^{14} W/cm^2 and 351-nm irradiation.[2] This demonstrates the effect of using smaller targets to achieve higher irradiation intensities.

It was shown in the prior measurements that the x-ray continuum spectrum for 351-nm irradiation reveals no evidence for "hot electrons" and that the "superhot electron" component is small.[5] The reported

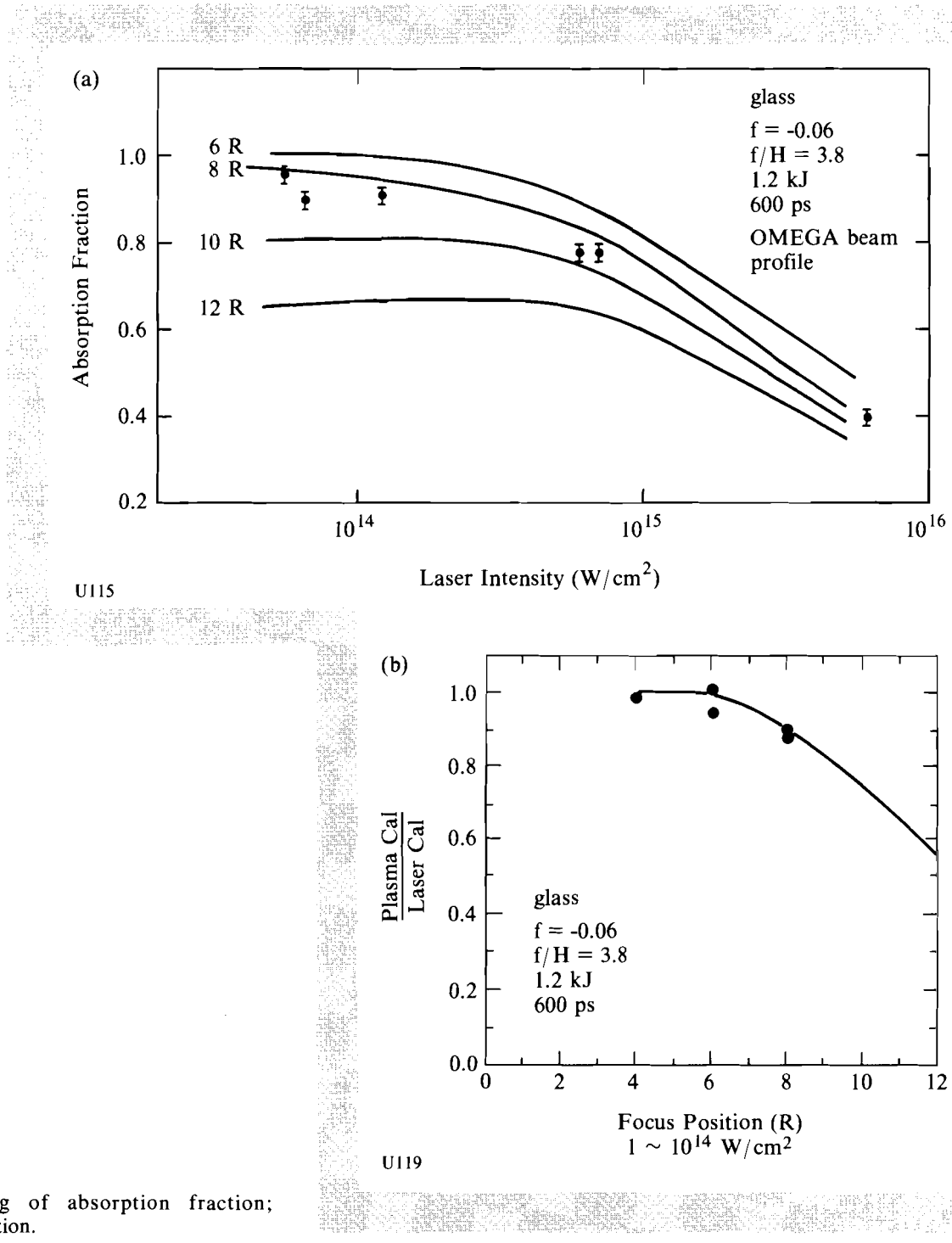

Fig. 31.7
(a) Scaling of absorption fraction;
(b) absorption.

fraction of incident energy in the superhot electrons is about 10^{-4}. It was decided to measure the total energy radiated into x rays. A differential x-ray calorimeter was constructed to make this measurement. (The sensitivity of this calorimeter is shown in Fig. 31.8.) The calorimeter has a flat sensitivity for x rays with energies less than 6 keV. At 6 keV, effects of the Ta L_3 absorption edge at 9.877 keV are evident. This detector is insensitive to the superhot

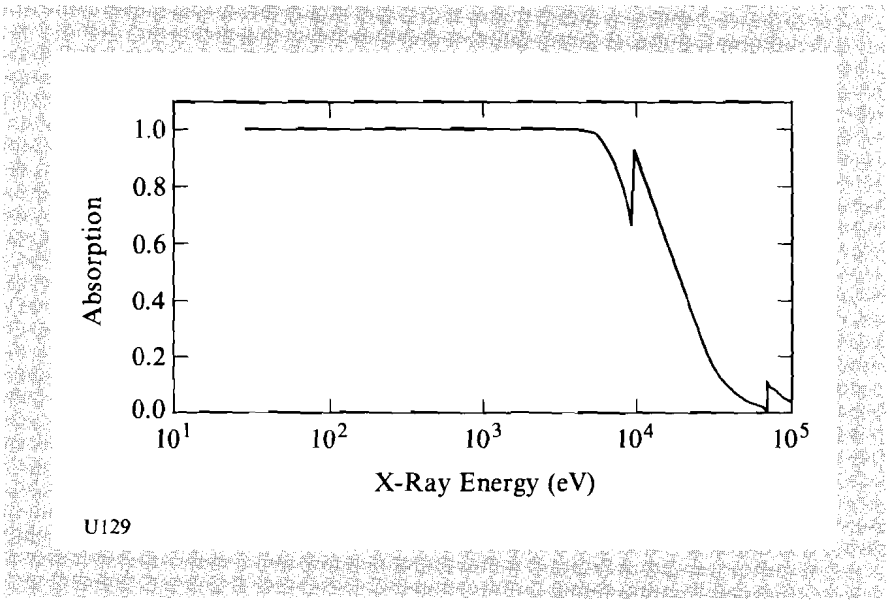

Fig. 31.8
X-ray calorimeter sensitivity.

electrons that radiate x rays with energies above 20 keV. The predominant contribution in the x-ray spectrum will come from silicon line emission and the low-energy continuum.

With the increased efficiency of energy absorption of targets when irradiated with shorter-wavelength lasers, the emission of soft x rays by the overdense plasma needs to be characterized. Figure 31.9 shows the percent of absorbed energy radiated into x rays as a function of incident-laser intensity for solid glass spheres. The circular points are the measured data and the square points are the predicted *LILAC* values for the experimental parameters. It is evident that there is good agreement between the experimental measurements and the theoretical calculations over the incident intensities from 6×10^{13} to 2×10^{15} W/cm^2. At these intensities, about 20% of the absorbed energy is converted to x rays.

X-ray radiation in *LILAC* is calculated with a multigroup line model. The group elements have been optimized for the hydrogen-like and helium-like lines in the silicon emission spectrum. The radiation transport is then done with the assumption of local thermodynamic equilibrium and look-up tables for the opacities. This calculation works well at predicting the x-ray fluence over a broad range of laser intensities.

The agreement between the *LILAC* calculations and the experimental measurements for solid glass targets is very good. The experiments have studied the coronal region of the plasma, where the majority of the laser energy is absorbed and where most of the line emission originates. The agreement between the calculations and the measured data indicate that the physics of the plasma corona is well understood. Since these are solid targets, the experiments are not complicated by the motion of the target surface. Thus, the plasma establishes a set of physical conditions that are relatively stationary and can be well modeled. Figure 31.10 shows that a stationary target surface is not

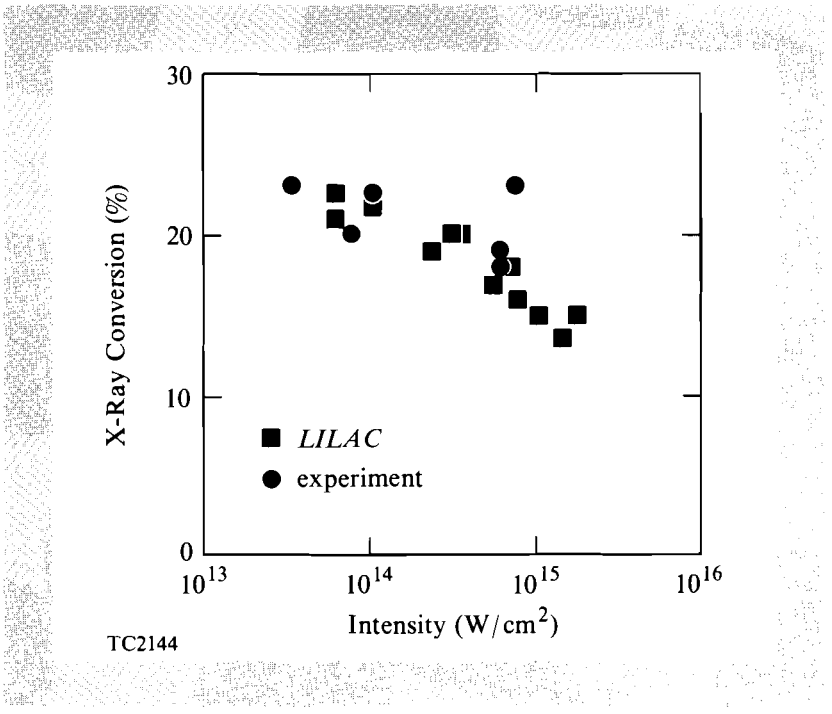

Fig. 31.9
Solid glass targets: x-ray conversion efficiency.

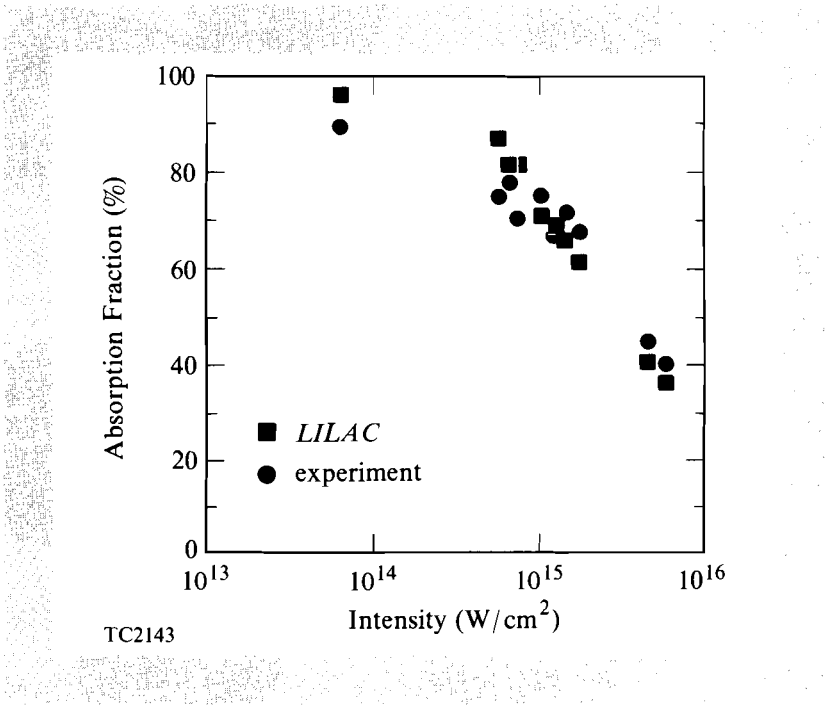

Fig. 31.10
Glass shell targets: absorption.

necessary for *LILAC* to predict measured absorption correctly. The absorbed energy fraction is plotted versus incident laser intensity. The round points are the experimental data and the square points are the *LILAC* predictions. The agreement is quite good and confirms that the coronal conditions of the laser-generated plasma are well understood in terms of the absorption of incident energy and the radiation of this energy into x rays.

ACKNOWLEDGMENT

This work was supported by the U.S. Department of Energy Office of Inertial Fusion under agreement No. DE-FC08-85DP40200, and by the Laser Fusion Feasibility Project at the Laboratory for Laser Energetics, which has the following sponsors: Empire State Electric Energy Research Corporation, General Electric Company, New York State Energy Research and Development Authority, Ontario Hydro, and the University of Rochester. Such support does not imply endorsement of the content by any of the above parties.

REFERENCES

1. W.C. Mead *et al.*, *Phys. Rev. Lett.* **47**, 1289 (1981).
2. W. Seka, R. S. Craxton, J. Delettrez, L. Goldman, R. Keck, R. L. McCrory, D. Shvarts, J. M. Soures, and R. Boni, *Opt. Commun.* **40**, 437 (1982).
3. C. Garban-Labaune *et al.*, *Phys. Rev. Lett.* **48**, 1018 (1982).
4. D. C. Slater *et al.*, *Phys. Rev. Lett.* **46**, 1199 (1981).
5. M. C. Richardson, R. S. Craxton, J. Delettrez, R. L. Keck, R. L. McCrory, W. Seka, and J. M. Soures, *Phys. Rev. Lett.* **54**, 1656 (1985).

1.C A Source of Hot Spots in Frequency-Tripled Laser Light

To achieve the high-density compressions required for thermonuclear ignition with direct-drive laser fusion, very smooth laser intensity profiles must be obtained in the target plane. Intensity variations around a smooth envelope must be less than about $\pm 10\%$. The effect of beam structure would be to implode some portions of the target faster than others and to "seed" the Rayleigh-Taylor hydrodynamic instability, resulting in reduced spherical convergence of the target, mixing between the shell and fuel, and a substantially degraded neutron yield. Considerable effort has been expended at LLE to determine the present quality of the OMEGA laser beams, and to determine what improvements might be necessary to meet the high-density milestones set for the OMEGA system. An important achievement of this uniformity program is that for the first time there is an understanding of what causes the observed laser-beam intensity variations in the target plane.

Detailed examination of the equivalent-target-plane (ETP) image of an OMEGA UV test beam has shown the presence of numerous hot spots with peak-to-valley variations of about 2 to 1 and spot widths of about 5% to 10% of the target diameter. The hot spots were found to occur only in focused, frequency-tripled UV light; they were relatively insignificant in the fundamental IR beam, which was dominated by long-wavelength structure (Fig. 31.11). The research effort to improve beam uniformity concentrated on identifying what aspect of the frequency-tripling process is responsible for the generation of the hot-spot structure. The answer was found by combining high-resolution

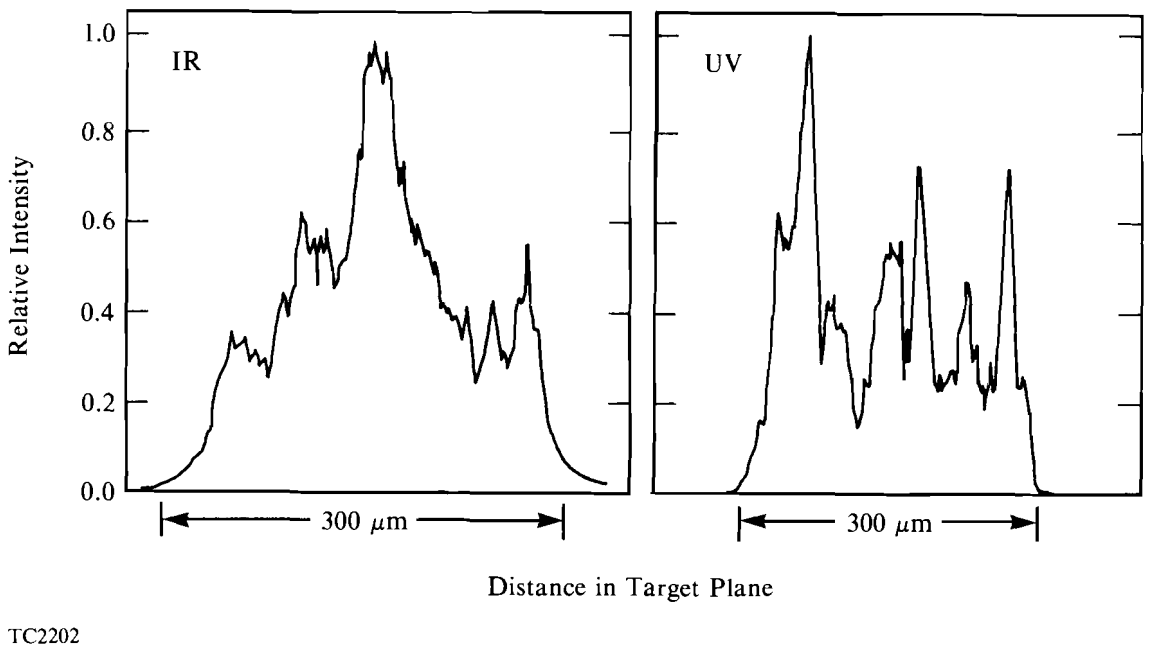

Fig. 31.11
Measured equivalent-target-plane (ETP) image for an IR beam and a frequency-tripled UV beam. Frequency tripling was observed to produce hot spots in the target-plane beam profile.

phase measurements of the near-field beam with computer modeling of the beam propagation to the target plane. The source of the hot spots lies in the phase error of the IR laser system, before conversion occurs.

Phase error is introduced by variations in the index of refraction Δn across the beam. The resulting variation in optical path length $\Delta\ell$ of rays with geometric path length ℓ is $\Delta\ell = \Delta n\ell$; the phase error is $\phi = k\Delta\ell$, where k is the wave number of the light. (Additional phase error can be introduced by variations in ℓ for different rays.) For a beam propagating in the z direction, the electric field depends on the phase error as $E(\text{IR}) \sim \exp[ik_o(z+\Delta\ell)]$, where the subscript o refers to IR light. The shape of the wave front is given by the term in parenthesis: $z+\Delta\ell$ = constant. During frequency conversion, the wave front is not changed; only the wave number is tripled—i.e., $E(\text{UV}) \sim \exp[i3k_o(zz+\Delta\ell)]$. A geometrical optics analysis would say that the UV and IR beams should show identical structure, since propagation is in the direction normal to the wave front, and they both have the same front. However, as the far field of the focusing lens is approached, diffractive effects will set in, and the two wavelengths of light will behave differently. If the phase error ϕ is sufficiently large, the beam will act as if it had been broken up into small beamlets, each with its own diffraction pattern; interference between the beamlets can lead to substantial hot spots. For the formation of beamlets to occur, the phase variation should be greater than about $2\pi/10$ rad and have a spatial variation smaller than about 1/10 the beam diameter. Since the phase error relative to the light wavelength is tripled upon frequency

conversion, IR phase errors as small as $2\pi/15 - 2\pi/30$ are enough to cause beamlet formation in the resulting UV-converted beam.

One of the 24 OMEGA beamlines was examined in detail to identify the sources of phase error. Phase errors can occur within the amplification chain, the frequency-conversion crystals, and the transport optics, as well as during beam propagation through the air to the target chamber. For high-efficiency frequency conversion, the UV light must have the same phase structure as the IR; the high optical quality of the conversion crystals in the test beam precluded the introduction of any additional, significant phase error during the frequency-tripling process. Also, no significant amplitude errors are introduced during conversion, as the measured near-field UV images show a relatively smooth profile (Fig. 31.12). Atmospheric turbulence was found to be one source of phase error that produced varying amounts of hot-spot structure. By enclosing part of the test beam in a corridor, thus isolating it from air fluctuations within the laser bay, some reduction in the hot-spot amplitude was observed, together with increased shot-to-shot reproducibility of the beam structure—though a major portion of the hot-spot structure still remained. Thus, for this beamline the damaging phase error must be inherent in the IR laser chain. These errors can be passive, due to imperfections in the amplifying medium and optical elements, or dynamic, due to variations in the index of refraction of amplifier glass arising from, for instance, thermal stress from flashlamp radiation. A high-resolution measurement of the IR near-field phase was made (as discussed in the article entitled "High-Power Laser Interferometry" appearing in this issue) to search for the small-scale structure that might lead to target-plane hot spots.

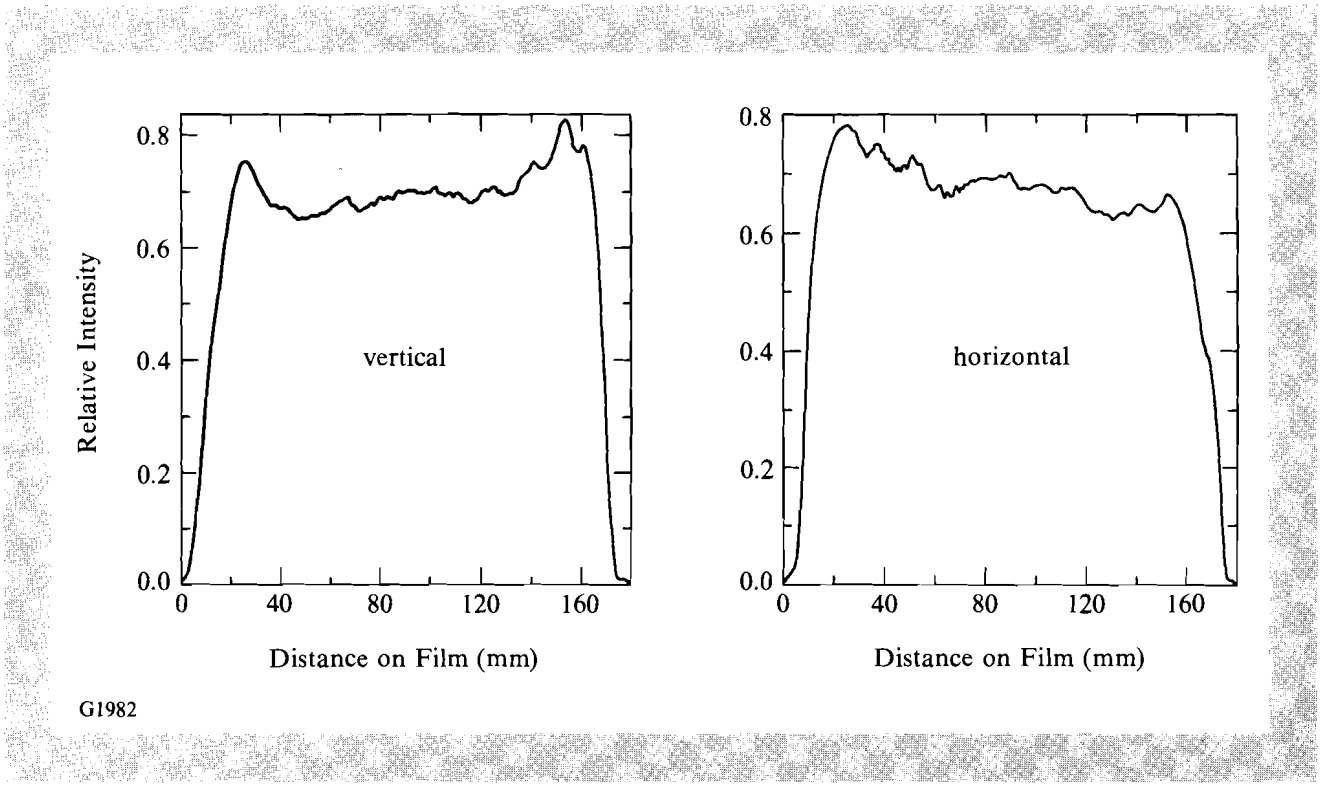

Fig. 31.12
Measured near-field UV image. No large amplitude variations were observed in the near field.

The effect of the near-field phase errors on the target-plane beam profile was determined by computer simulation of the beam propagation. The numerical model treated the laser propagation according to scalar diffraction theory using Kirchhoff-Huygens boundary conditions. Each component of the laser electric field at a point $\boldsymbol{r}$ is described by the scalar quantity $U(\boldsymbol{r})$ and is related to the near-field amplitude A and phase according to[1]

$$U(\boldsymbol{r}) = -i\frac{F}{\lambda}e^{-ikF}\int e^{ik(d+\Delta\ell)}A\,d\Omega/d \quad , \tag{1}$$

where the integration is over the near-field aperture, F is the lens focal length, and d is the distance to the point $\boldsymbol{r}$ from a point $\boldsymbol{R}$ on the lens (Fig. 31.13). Following Born and Wolf, we make the following approximation:

$$d-F = \hat{\boldsymbol{q}} \cdot \boldsymbol{r}$$

appropriate near the focal plane ($r/F << 1$), but not necessarily in the far field. Equation (1) simplifies to

$$U(\boldsymbol{r}) = -\frac{i}{\lambda}\int e^{-ik(\hat{\boldsymbol{q}}\cdot\boldsymbol{r}-\Delta\ell)}A\,d\Omega \quad . \tag{2}$$

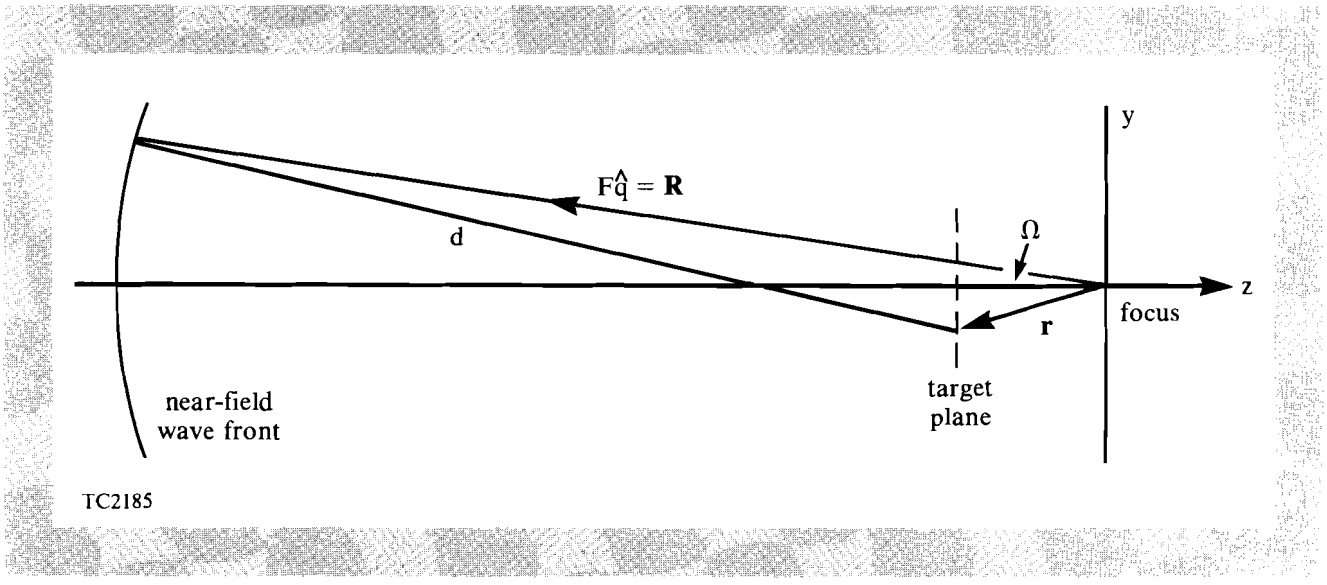

Fig. 31.13
Geometry and variables used in the beam propagation calculation.

The coordinates of $\boldsymbol{r}$ and $\boldsymbol{R}$ are defined to be (x,y,z) and (X,Y,Z), respectively. Since the point $\boldsymbol{R}$ lies on a spherical wave front of radius F, the value of Z is $Z = -(F^2 - X^2 - Y^2)^{1/2}$, which is approximated by

$$Z = -F\left[1-\frac{1}{2}(X^2+Y^2)/F^2 \ldots\right] \quad . \tag{3}$$

Keeping the first two terms in brackets is the Fresnel approximation, which is appropriate for the quasi-near-field plane, where OMEGA targets are positioned.

Equation (2) was solved by dividing the near-field aperture into a 100 × 100 square computational grid. The amplitude A and phase ϕ were assumed to be constant in each computational cell. Combining Eq. (3) with Eq. (2) yields

$$U(r) = -\frac{i}{\lambda}\sum_{i,j} A_{i,j}\, e^{-ik(\Delta\ell_{ij}-z)} \times \int_i e^{-ik(xX/F-\frac{1}{2}z\,X^2/F^2)}dX \times \int_j e^{-ik(yY/F-\frac{1}{2}zY^2/F^2)}dY \quad . \tag{4}$$

The X and Y integrations are across cell ij, from X_i to X_{i+1} and Y_j to Y_{j+1}, respectively. The integrations were written in terms of the standard Fresnel integrals and were evaluated from numerical tables. The target-plane laser intensity is then proportional to $|U(r)|^2$.

The near-field amplitude and phase are inputs to the propagation code. The near-field amplitude profiles of Fig. 31.12 were typical of all shots, for both the IR and UV, having intensity modulations of $\pm 10\%$. Very little structure is observed; in fact, the amplitude could be replaced by a smooth supergaussian in the code with very little effect on the calculated TP image—i.e., phase error completely dominates the beam structure. An example of the measured phase error for two perpendicular cuts through the beam is shown in Fig. 31.14. The long-wavelength structure is responsible for shifting the position of the beam and distorting its general shape, as seen in the IR image in Fig. 31.11. The small-scale structure has relatively low modulation, but this is the source of the UV hot spots.

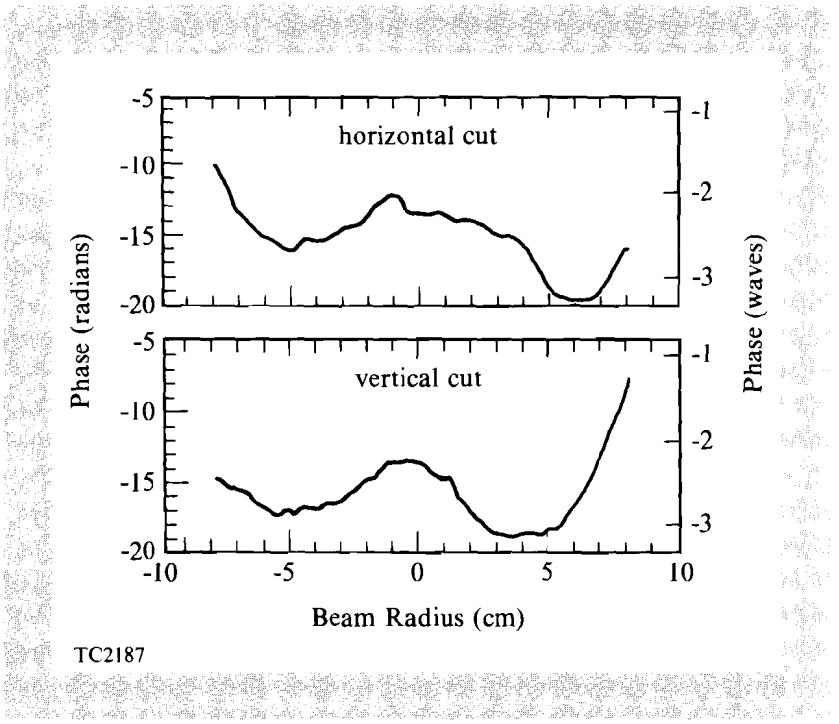

Fig. 31.14
Measured near-field phase error. Some small-scale structure is visible, and this leads to hot-spot formation. The phase was measured in the IR and has been multiplied here by 3 for the UV calculation.

A comparison between a calculated IR target-plane image and a measured ETP image is shown in Fig. 31.15. The characteristic features of the profile have been reproduced, specifically, the central peak and its width, and in the horizontal cut the shift of the central peak and the appearance of a peak on the edge. The last feature is the only structure predominantly caused by the near-field amplitude, which had one edge slightly more intense than the rest of the beam. A supergaussian near-field amplitude with the measured phase error reproduces all the structure except that one edge peak.

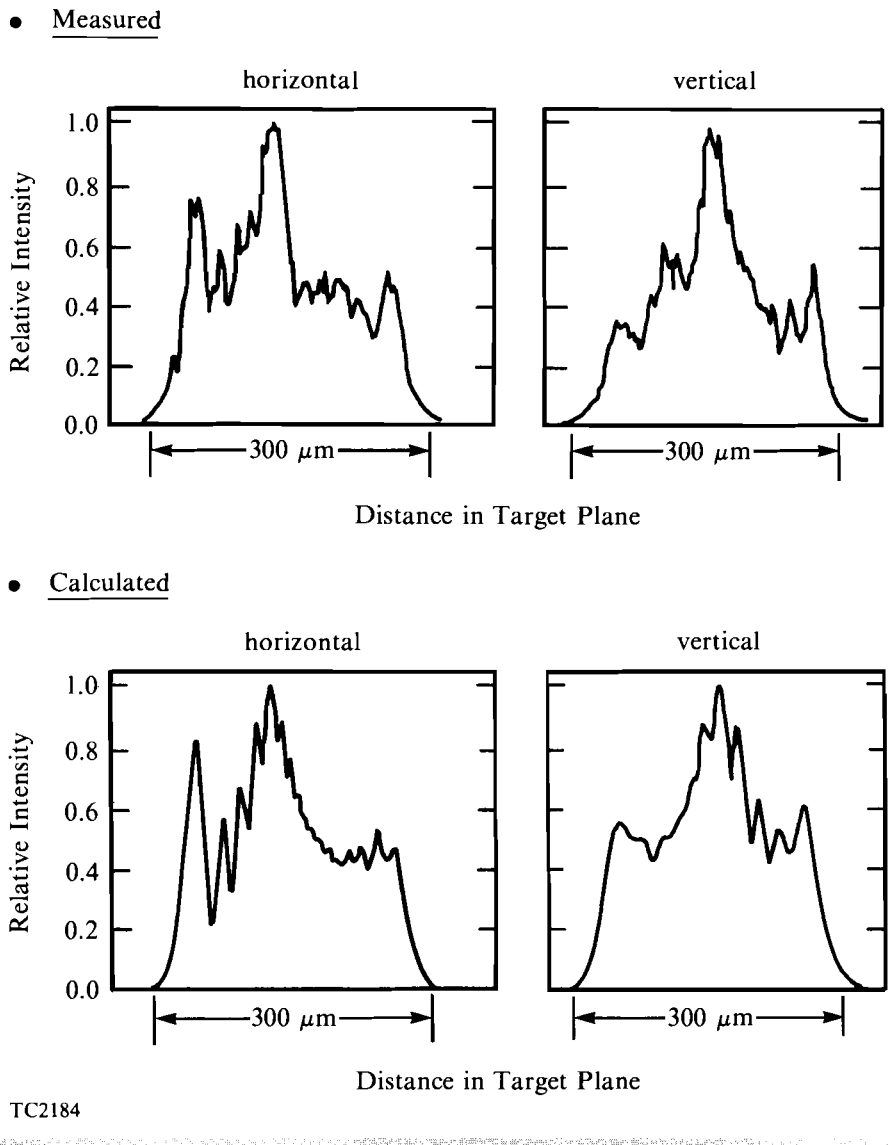

Fig. 31.15
Using measured near-field amplitude and phase variations, an IR target-plane profile was calculated. The general features of the measured ETP image have been reproduced.

The main question is whether the phase error can simultaneously account for the structure in both the IR and UV target-plane images. The result is shown in Fig. 31.16. A supergaussian near-field amplitude was used to demonstrate unequivocally that the hot-spot formation is primarily dominated by phase error. The same phase error was used in both the UV and IR calculations, the only difference in the calculations being the wavelength of the light. Comparing Figs. 31.11 and 31.16, we see that the observed beam breakup into hot spots, in going from the IR to the UV, has been well reproduced.

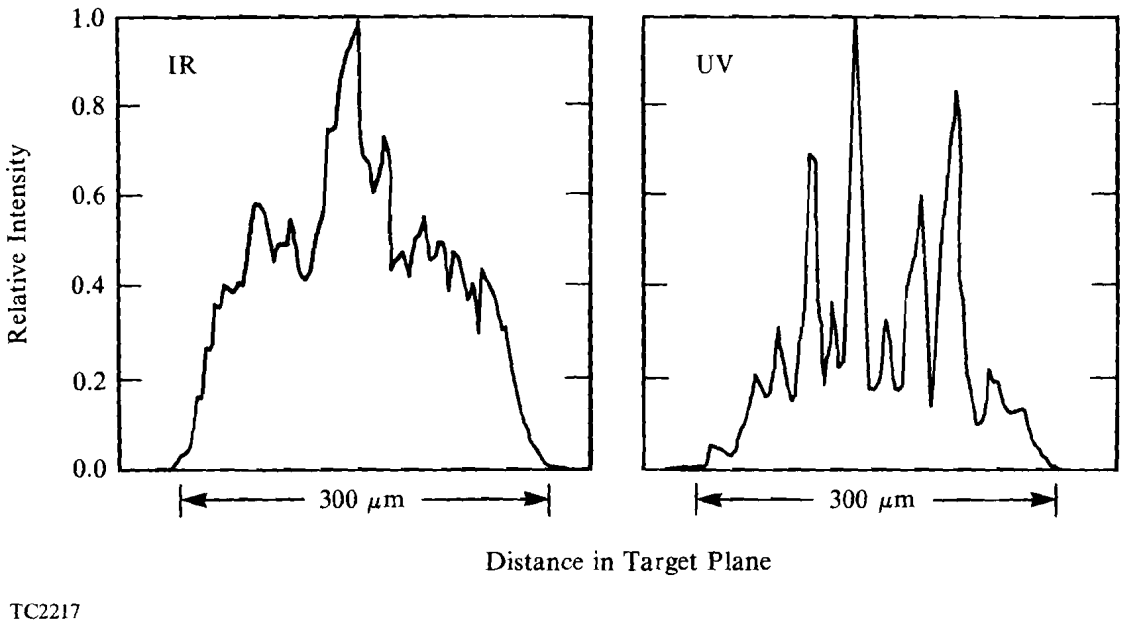

Fig. 31.16
Calculated target-plane images for an IR and a UV beam. Both calculations used the same near-field amplitude (supergaussian) and the same measured phase error (Fig. 31.14); only the light wavelength was different. The IR image is slightly different than the one shown in Fig. 31.15 because a different set of phases and amplitudes was used. Hot-spot structure is produced in the UV but not in the IR calculation, in agreement with the experimental observation (Fig. 31.11).

The breakup of the UV beam appears to be the result of small-scale-length phase errors. When the phase error exceeds about $2\pi/10$, the beam effectively breaks up into separate beamlets. Similar behavior was found computationally by imposing a 10 x 10 square random-phase mask on a beam with otherwise perfect phase. The phase of each cell in the mask was chosen randomly between 0 and $2\pi/3$. This configuration produced hot-spot structure similar to that seen in the UV target-plane image. When the phase error was reduced by a factor of 3 for the corresponding IR calculation, the hot-spot structure disappeared.

As a result of combining high-resolution phase measurements with computer modeling, the reason for the appearance of the hot-spot structure in the UV beam (and its absence in the IR) is now well understood. The code is now being used to investigate various strategies for improving beam uniformity, such as random-phase masks.

ACKNOWLEDGMENT

This work was supported by the U.S. Department of Energy Office of Inertial Fusion under agreement No. DE-FC08-85DP40200, and by the Laser Fusion Feasibility Project at the Laboratory for Laser Energetics, which has the following sponsors: Empire State Electric Energy Research Corporation, General Electric Company, New York State Energy Research and Development Authority, Ontario Hydro, and the University of Rochester. Such support does not imply endorsement of the content by any of the above parties.

REFERENCES

1. M. Born and E. Wolf, *Principles of Optics*, 6th ed. (Pergamon Press, Oxford, 1986), pp. 436–437.

Section 2
ADVANCED TECHNOLOGY DEVELOPMENTS

2.A High-Power Laser Interferometry

Central to the uniformity issue is the need to determine the factors that control the target-plane intensity distribution of the 24 OMEGA UV laser beams. The extent to which they can be controlled will determine overall target irradiation uniformity. Wave-front measurement and analysis techniques have generated accurate near-field intensity and phase, and target-plane intensity distributions of individual laser beams. Direct-phase measurements have uncovered phase structures in the UV beams that are responsible for hot spots on target. They have revealed the relative importance of the nonuniformity sources that affect the intensity modulation on the target surface. High-power laser interferometry is a key technological advancement in solid-state laser development and in the understanding of laser-beam focusability.

Phase-Front Recording and Reconstruction

Expressions describing the interference between test and reference beams show the means by which the phase is extracted from a high-carrier-frequency interferogram. Let the test-beam wave and reference wave be represented by

$$T(x,y)\cos\left[-\omega t + kx\sin(\alpha/2) + ky\sin(\gamma/2) + \psi(x,y)\right] \quad \text{(test)} \qquad (1)$$

and

$$R(x,y)\cos\left[-\omega t - kx\sin(\alpha/2) - ky\sin(\gamma/2) + \phi(x,y)\right], \quad \text{(reference)} \qquad (2)$$

where $T(x,y)$, $\psi(x,y)$, and $R(x,y)$, $\phi(x,y)$ represent the amplitude and phase distributions of the electric fields. The propagation constants, $\pm\, k x \sin(\alpha/2)$ and $\pm\, k y \sin(\gamma/2)$, represent symmetric interference about the x and y axes (see Fig. 31.17). The temporal frequency ω has units of radians/second. Square-law detection of the interference between the two waves produces a signal represented by

$$S(x,y) = T^2(x,y) + R^2(x,y) + \frac{T(x,y)R(x,y)}{2} e^{i[2kx\sin(\alpha/2) + 2ky\sin(\gamma/2)+\psi(x,y)-\phi(x,y)]} + \frac{T(x,y)R(x,y)}{2} e^{-i[2kx\sin(\alpha/2) + 2ky\sin(\gamma/2)+\psi(x,y)-\phi(x,y)]} . \quad (3)$$

The above expression describes the linearly recorded interferogram. Complex notation of the oscillatory interference term shows holographic phase-front storage of the two wave fronts. Phase-front reconstruction is achieved through computerized image processing.

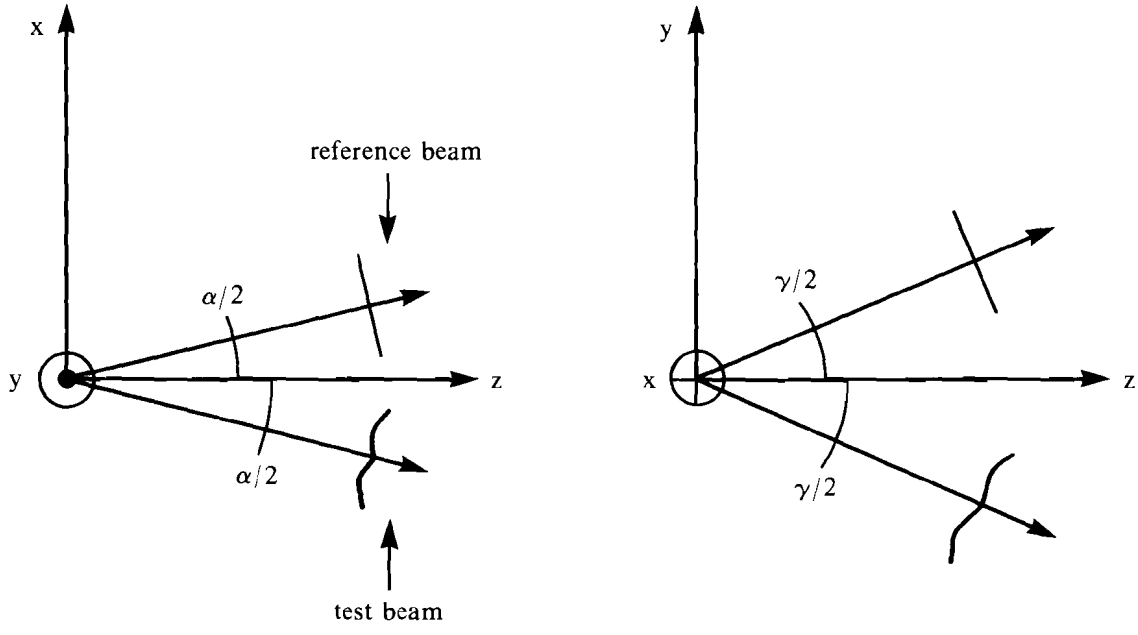

Fig. 31.17
Two-beam interferometry involves the coherent addition of a test beam and an appropriately produced, separate reference beam. The resulting interference pattern represents wavelength contours of the optical path difference between the two waves. In the case of a perfect plane-wave reference, the fringes represent wavelength contours of the aberrated test beam. Normally, a tilt component between the two beams is added to provide a carrier frequency for visual inspection or direct digitization. The values of α and γ are very small for interferometry but increase to a maximum value of π for holography.

Synchronous phase detection[1,2,3] in the spatial domain, rather than the time domain, brings interferometric analysis into the field of digital image processing. Assuming that the variations in the phase distributions, $\psi(x,y)$ and $\phi(x,y)$, are sufficiently sampled, Fourier analysis can be accurately performed on the intensity distribution $S(x,y)$. Fourier analysis is accomplished with greater ease by the substitution of the carrier-frequency parameters

$$\omega_o = 1/d_x = 2\sin(\alpha/2)/\lambda \text{ and } \nu_o = 1/d_y = 2\sin(\gamma/2)/\lambda$$

represented by

$$S(x,y) = T^2(x,y) + R^2(x,y) + \frac{T(x,y)R(x,y)}{2} e^{i[2\pi(\omega_o x + \nu_o y + \psi(x,y) - \phi(x,y)]} + \frac{T(x,y)R(x,y)}{2} e^{-i[2\pi(\omega_o x + \nu_o y + \psi(x,y) - \phi(x,y)]} . \quad (4)$$

The signal $S(x,y)$ is appropriately stored in the computer as a complex 2-D digital image, since an imaginary component forms during image manipulation. A complex 2-D Fourier transform of $S(x,y)$, defined as

$$F[S(x,y)] = s(\omega,\nu) \equiv \int_{-\infty}^{\infty}\int S(x,y)\, e^{-i2\pi(x\omega+\nu y)}\, dxdy , \quad (5)$$

is performed with an array-processor-enhanced, 2-D fast-Fourier-transform (FFT) algorithm. The image in the Fourier domain can be expressed as

$$s(\omega,\nu) \propto \boldsymbol{b}(\omega,\nu) + \boldsymbol{t}(\omega-\omega_o,\nu-\nu_o) \ast\ast \boldsymbol{r}^*(\omega-\omega_o,\ \nu-\nu_o) + \boldsymbol{t}^*(\omega+\omega_o,\nu+\nu_o) \ast\ast \boldsymbol{r}(\omega+\omega_o,\ \nu+\nu_o), \quad (6)$$

where $B(x,y) \propto T^2(x,y) + R^2(x,y)$; $\boldsymbol{b}$, $\boldsymbol{r}$, and $\boldsymbol{t}$ represent the Fourier transform of B, R, and T respectively; * denotes complex conjugation and $\ast\ast$ denotes a 2-D convolution. The first term $\boldsymbol{b}(\omega,\nu)$ represents the "zero-order" component, or background signal. Each of the two other terms contains the relevant phase information. Fourier side-lobe filtering is performed to extract one of the phase-front terms from all of the other information. Assuming nonoverlapping Fourier components, the side lobe is extracted with a rect(ω) rect(ν) window and shifted to the origin (see Fig. 31.18). This is represented by

$$s_F(\omega,\nu) \propto \delta(\omega+\omega_o,\ \nu+\nu_o) \ast\ast \left\{ s(\omega,\nu) \times \text{rect}\left[\frac{\omega-\omega_o}{\Delta\omega_c} , \frac{\nu-\nu_o}{\Delta\nu_c} \right] \right\}, \quad (7)$$

where $\Delta\omega_c$ and $\Delta\nu_c$ are spectral widths of the desired side-lobe filter, centered on the carrier frequencies ω_o and ν_o. Again, using an FFT

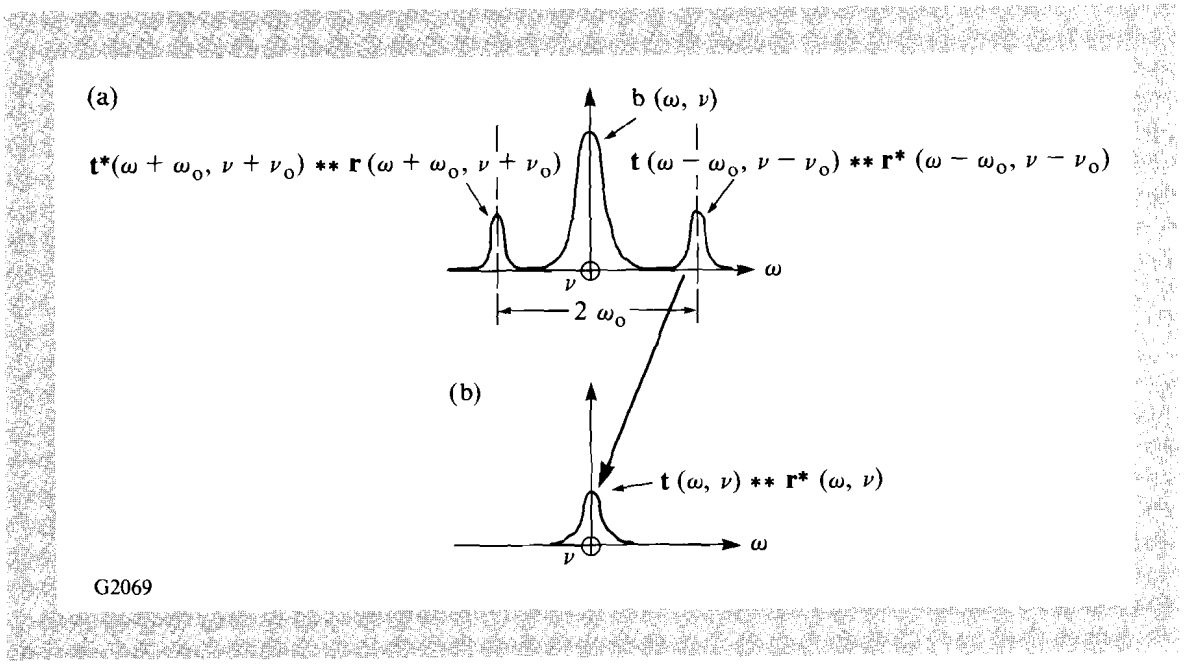

Fig. 31.18
The separated 2-D Fourier spectra (a) associated with the high-frequency interferogram. The left and right lobes both contain the required phase information and are symmetric about the origin. A window function is used to select the right lobe and shift it to the origin, thus removing all tilt from the recovered phase distribution. Experimentally, the carrier frequency is chosen to minimize overlap between the beam's power spectrum and the encoded phase.

algorithm, a reverse Fourier transform returns the analysis to the spatial domain, represented by

$$S_F\,(x,y) = \frac{T(x,y)R(x,y)}{2}\; e^{i[\psi(x,y)-\phi(x,y)]} \quad . \tag{8}$$

Taking a complex logarithm yields

$$\log\,\{S_F(x,y)\} = \mathrm{Log}\left[\frac{T(x,y)R(x,y)}{2}\right] + i\left[\psi(x,y)-\phi(x,y) + 2N\pi\right], \tag{9}$$

where the imaginary component is the recovered phase difference between the test and reference beams. Since the digital interferogram is stored as a complex image, it is necessary to calculate only an arc tangent function,

$$\psi(w,y)-\phi(x,y) = \tan^{-1}\left\{\frac{\mathrm{Real}[S_F\,(x,y)]}{\mathrm{Im}[S_F\,(x,y)]}\right\} . \tag{10}$$

The arc tangent function subroutine operates over only the principal branch ($N=0$) with $-\pi < \theta < \pi$; thus, each pixel of the phase image is undetermined by a multiple of 2π. These discontinuities are corrected by appropriately shifting adjacent pixels by 2π.

An overlapping of the Fourier spectra of each of the background signals reduces the reconstructed phase-front accuracy. The effects of

Fourier-spectrum overlap can be reduced by locating the carrier frequency at a minimum of the background power spectrum. High-power laser-beam, phase-front analysis, approaching $\lambda/50$, has been achieved. Accuracies greater than $\lambda/100$ can be achieved by properly dealing with image discontinuities.[4]

Laser Interferometry

Uniformity measurements have been advanced by the design of a new beam-diagnostic package that includes photographic recording of the near-field and equivalent-target-plane intensity distributions, as well as phase-front measurement by self-generated reference-beam interferometry. Self-generated reference-beam interferometry involves the creation of a separate reference beam from the test beam.[5] Rewriting Eq. 8 to include the generation of a reference beam, we obtain

$$S_F(x,y) = \frac{T(x,y)T(xM,yM)}{2} e^{i[\psi(x,y)-\psi(xM,yM)]} . \quad (11)$$

Radial shearing interferometry is performed when the magnification M is about 1 to 10. However, as M approaches 100, two-beam interferometry can be performed. There must exist a region of the test beam over which the phase error changes by no more than the desired phase-front accuracy.

Figure 31.19 schematically illustrates the way in which two beams are produced using a parallelogram Mach-Zehnder configuration. The test beam is down collimated in one arm of the system, while a high-

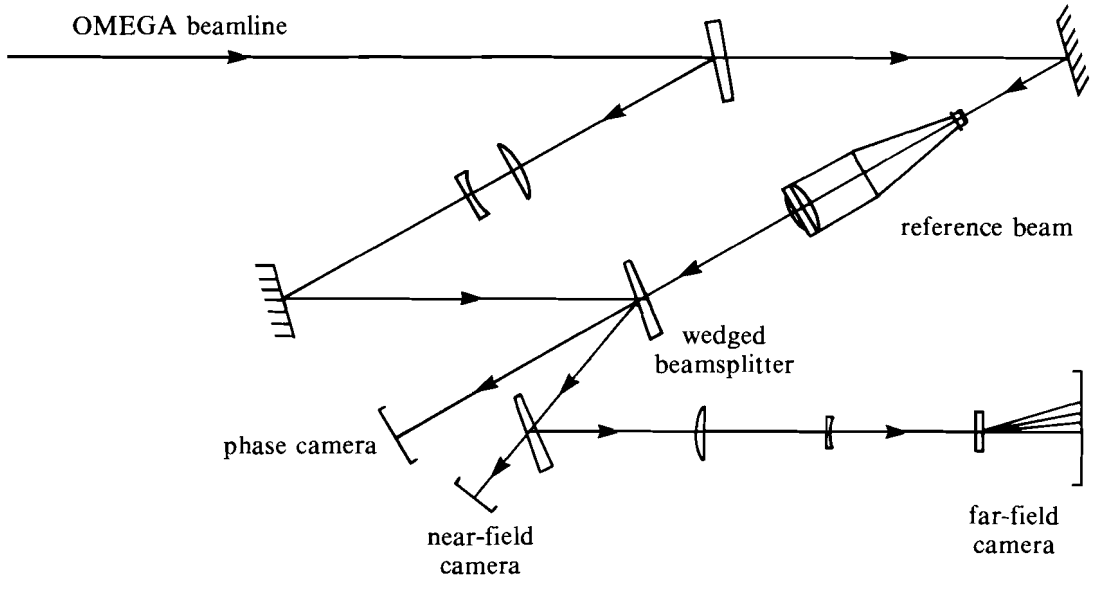

Fig. 31.19
A parallelogram Mach-Zehnder interferometer, used to measure the phase front of a high-power, solid-state laser beam, includes a self-generated reference beam in one arm and a down-collimated test beam in the other. Near-normal incidence of reflection reduces the sensitivity to polarization-dependent phase fronts. The position of the reference-beam collimator is varied for spatial selection of the reference or to study coherence effects. The angle of the recombining beam splitter can be varied throughout the interferometry to holography ranges.

quality, coherent reference is created from a sufficiently small region of the transmitted test beam in the other arm. Two-beam interference is formed by the recombining beam splitter such that the fringe frequency is variable over the interferometry to holography ranges, i.e., the angle between the two wave fronts varies from 0° to 180°. Near-normal incidence is used on the two bare-surface beam splitters to prevent polarization sensitivity. Conventional photographic methods are used to record the interferometric intensity distributions.

OMEGA Phase Analysis

High-power laser interferometry and high-resolution fringe analysis have been applied to beamline 6-2 of the OMEGA laser system. Initially, interferograms were generated with a low tilt-fringe frequency, sufficient for an analysis consisting of intensity subtraction and hand digitization of the fringe contour peaks. Figure 31.20 shows the various images involved in this routine. The near-field intensity [Fig. 31.20(a)] and interferogram [Fig. 31.20(b)] were first digitized on a microdensitometer. An offset and a multiplier of the near-field intensity are subtracted from the original interferogram to provide an enhanced fringe pattern [Fig. 31.20(c)]. The fringe contour peaks are hand digitized, producing between 100 to 200 data points that are least-square fit to an eighth-order Zernike polynomial. A contour of the detected phase is shown in Fig. 31.20(d). Hand digitization and analysis were repeated to demonstrate a reproducibility of approximately $\lambda/15$. However, $\lambda/15$ accuracy and a few-hundred-point resolution did not account for the intensity modulations that were observed with UV equivalent-target-plane photography.

Phase-front measurements of beamline 6-2 were repeated with spatial synchronous phase detection. Figure 31.21 is a flow chart describing the image manipulation of the high-frequency interferogram. A measurement accuracy of $\lambda/50$ over an image area of 256×256 pixels was achieved. With this measurement, diffraction modeling, involving computerized beam propagation of the near-field amplitude and phase distributions, established that the irradiation uniformity level on target is dominated by the phase front of the individual beams. In particular, the high-frequency components were responsible for most of the nonuniformity (see the article in this issue entitled "A Source of Hot Spots in Frequency-Tripled Laser Light"). Interferometric analysis of the pulsed-laser radiation and the individual components of a beamline has identified the major sources of phase modulation. Practical limitations on the homogeneity of glass and crystals and on surface figuring indicate that all optical elements contribute phase errors to a laser beamline. It is the 2-D accumulation of these phase errors, from large numbers of optical elements, that statistically degrades the beam's phase front. In addition, the reproducibility of the phase front is affected by dynamic sources of phase modulation, such as atmospheric turbulence and pump-induced amplifier stress.

The major thrust in the areas of phase-front measurements and improvements to the OMEGA laser involves distinguishing the reproducible and irreproducible components of the phase front. Figure 31.22 shows preliminary results of high-resolution phase

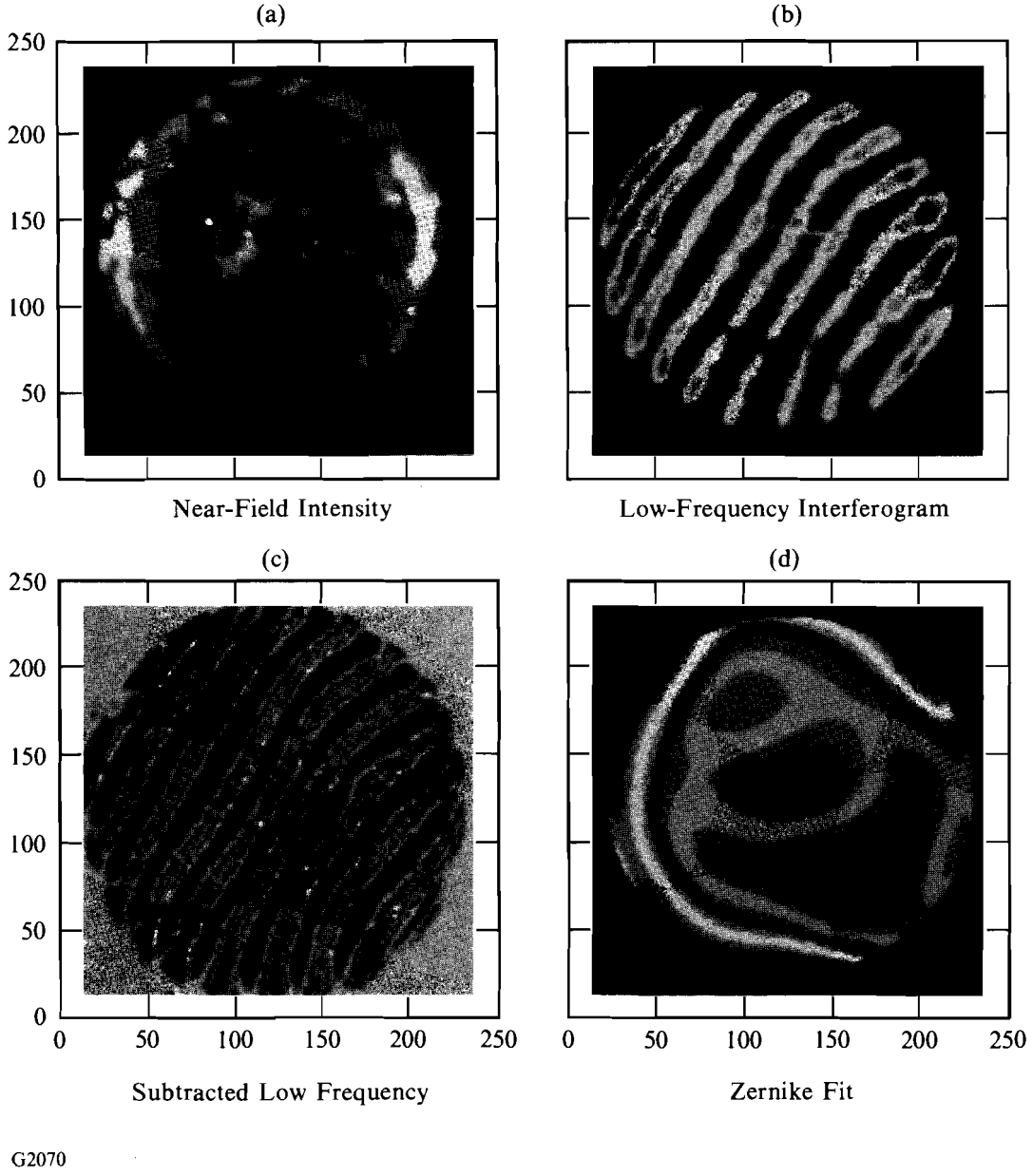

Fig. 31.20
For visual inspection or hand digitization of the contour peaks, a tilt component corresponding to a dozen fringes over the beam diameter is selected (b). The phase front of the beam is encoded within the fringe contours of the interferogram. Enhanced fringes (c) are obtained by subtracting the near-field intensity (a) from the original interferogram. Hand digitization of the contour peaks is followed by an eighth-order Zernike-polynomial least-squares fit to the data points. Repeated digitization and analysis have indicated an accuracy of approximately $\lambda/15$. Smooth contours of phase (d) are an indication of the bandpass limit associated with an eighth-order polynomial fit to hand-digitized data.

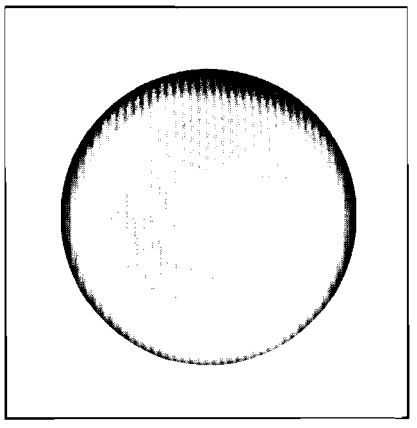

High-Frequency Interferogram

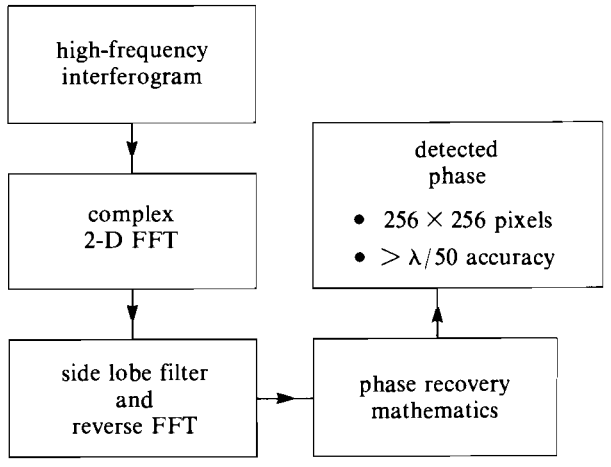

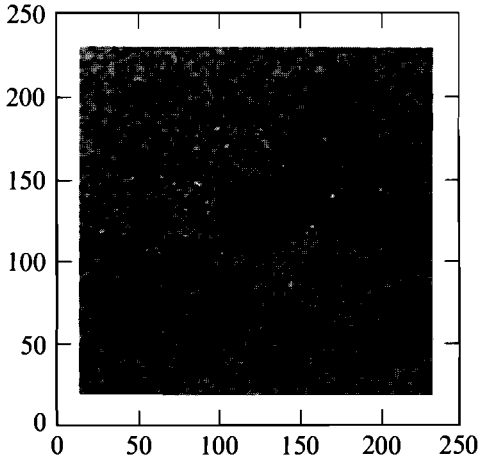

2-D FFT of Interferogram

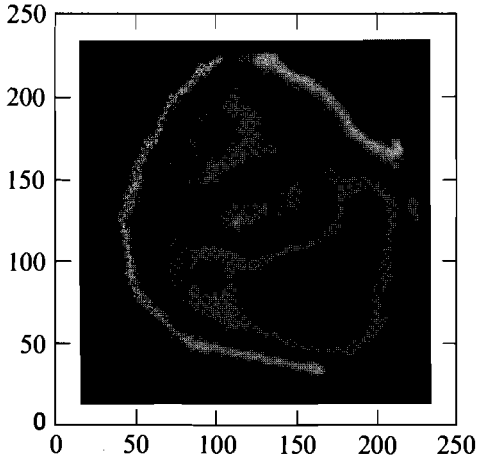

Detected Phase
(λ/7 contour level)

G1979

Figure 31.21
Spatial synchronous phase detection (SSPD) makes possible the application of phase-shifting interferometry to high-power pulsed radiation. A large tilt is introduced between the test and reference beams to produce a high-frequency interferogram. Fourier analysis of this complex image provides a method for eliminating the amplitude errors associated with direct-fringe digitization. SSPD offers a measurement accuracy of greater than λ/50 over an image area of 256 × 256 pixels. The detected phase (lower right) shows the high-frequency phase information that is recovered from SSPD analysis. Comparison with Fig. 31.20 shows the increased phase bandpass. Subsequent modeling showed that phase features as small as λ/30 (λ = 1.054 μm) are responsible for intensity nonuniformities on target.

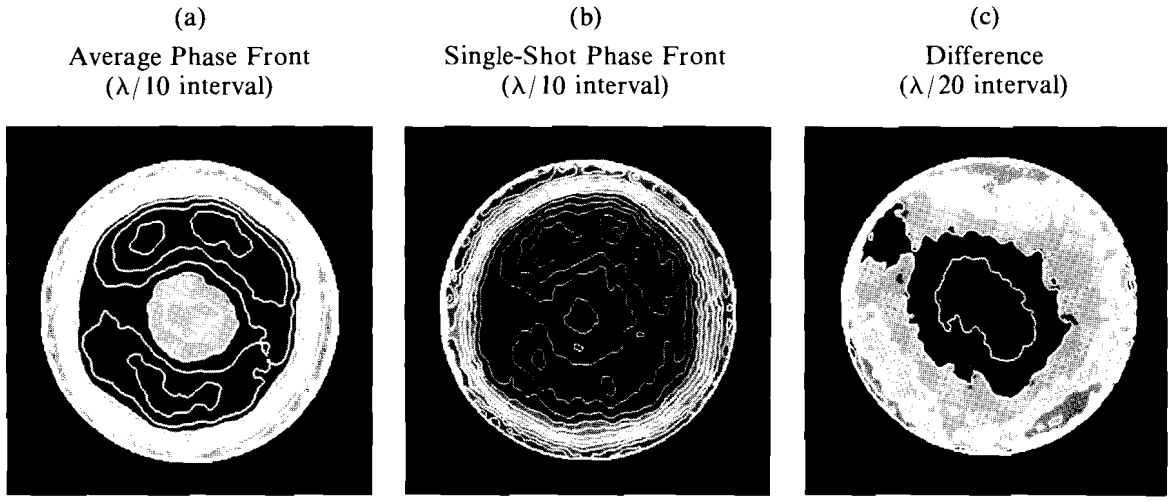

Figure 31.22
Phase-front reproducibility is essential for static phase correction. The difference (c) between a single driver-line shot (b) and an average of six shots (a) is substantially lower in phase distortion than for any one shot. Reproducibility can be increased through amplifier development and turbulence control.

measurement of the driver line. A large reproducible component of the phase front indicates that phase-correction technologies can improve driver-line performance. Once the irreproducible phase effects are reduced or eliminated, the feasibility of phase correction strategies can be fully assessed. Conventional glass phase plates and holographic corrector elements are currently under investigation. In addition, spatial filtering experiments are being conducted to determine the practical limits of eliminating the high-frequency phase components.

Future Applications

High-power laser interferometry will be applied to all of the OMEGA beamlines following diagnostic development and improvements to the synchronous-detection algorithms. This powerful tool will also aid in the characterization of cryogenic-target fuel layers. Time-dependent phase effects in lasers and laser amplifiers can be studied with electronic spatial-synchronous phase detection. Furthermore, filamentation studies of underdense plasmas, using an optical probe, can be enhanced with high-resolution interferometry.[6]

Summary

Self-generated reference beam interferometry has been successfully implemented on an OMEGA high-power laser beam. Spatial-synchronous phase detection is an image-processing-based analysis technique that provides high-resolution phase-front reconstruction. Together, these developments make it possible to perform phase-shifting interferometry on high-power pulsed radiation. Furthermore, with this measurement technique, diffraction modeling has provided a

clear understanding of the importance of small-scale phase structures to the irradiation uniformity on target.

ACKNOWLEDGMENT

This work was supported by the U.S. Department of Energy Office of Inertial Fusion under agreement No. DE-FC08-85DP40200, and by the Laser Fusion Feasibility Project at the Laboratory for Laser Energetics, which has the following sponsors: Empire State Electric Energy Research Corporation, General Electric Company, New York State Energy Research and Development Authority, Ontario Hydro, and the University of Rochester. Such support does not imply endorsement of the content by any of the above parties.

REFERENCES

1. Y. Ichioka and M. Inuiya, *Appl. Opt.* **11** (1972).
2. M. Takeda, H. Ina, and S. Kobayashi, *J. Opt. Soc. Amer.* **72**, 156 (1982).
3. K. H. Womack, *Opt. Eng.* **23**, 391 (1984).
4. T. Kessler, M.S. thesis, University of Rochester, 1984.
5. C. Roddier and F. Roddier, *Appl. Opt.* **26**, 1668 (1987).
6. K. A. Nugent, *Appl. Opt.* **24**, 3101 (1985).

2.B En Route to the Petawatt

Short-Pulse Amplification: the CPA Concept

In order to amplify short optical pulses, three major requirements have to be fulfilled by the amplifying medium. First, the bandwidth of the amplifier must be large enough to accommodate the full spectrum of the short pulse. Second, to efficiently extract the energy stored in the amplifier, the fluence of the pulse has to be near the saturation fluence of the medium $F_s = h\nu/\sigma$, where σ is the stimulated emission cross section. Finally, the intensity within the amplifier has to stay below a critical level at which nonlinear effects become significant and distort the spatial and temporal profiles of the pulse. The integrated nonlinear index along the optical path is given by the B integral[1]:

$$B = \frac{2\pi}{\lambda} \int \frac{\Delta n}{n}\, dl = \frac{2\pi}{\lambda}\, n_2 \int_o^L I(z)dz\ . \qquad (1)$$

The B integral at any position across the beam gives the amount of phase delay experienced by the high-intensity beam. The critical intensity corresponds to a B value of the order of 5. Above this value, the high spatial frequencies are preferentially amplified and must be removed by spatial filtering. In the case of dyes and solid-state media, this leads to a critical intensity of the order of 10 GW/cm^2.

Typically, dye and excimer systems are used to amplify short pulses. These media have broad bandwidths of the order of 20 nm, which can support pulse widths as short as 30 fs. However, these media have low

saturation fluence levels of millijoules per square centimeter. One-hundred-femtosecond pulses can be amplified to the saturation level without reaching prohibited peak powers and generating unwanted nonlinear effects. Dye amplifiers are therefore well suited for amplification of short pulses to the millijoule level. Further amplification of these pulses has been accomplished with excimer amplifiers[2] by scaling up the amplifier aperture.

As shown above, low saturation fluence combined with a short storage time of a few nanoseconds makes dyes and excimers less than ideal amplifier media. By using an amplifying medium with a thousand times larger saturation fluence, joule energies can be reached with a tabletop-sized system. For example, solid-state media doped with neodymium, chromium, or titanium typically have a saturation fluence of the order of 5 J per square centimeter. Furthermore, they can accept doping concentrations higher than 5×10^{20} atoms per cubic centimeter. Chromium-doped crystals have already shown lasing capabilities from 100 nm to 1100 nm with large bandwidths. One of them, alexandrite, with a bandwidth covering the 700-nm to 800-nm range, has reached a high-average-power performance of 100 W.[3] Another very promising medium is titanium-sapphire, which has been reported to lase between 700 nm and 1000 nm. A well-developed and widely used solid-state amplifier is neodymium glass. With a bandwidth larger than 20 nm, it can support the amplification of 100-fs pulses. However, if we amplify a 1-ps pulse to the saturation level, the power density becomes of the order of TW/cm^2, well above the critical intensity level. Because of the peak intensity limitation, the large amount of stored energy in this medium cannot be extracted. For this reason, solid-state lasers have been primarily used for long (nanosecond) pulse amplification, rather than for the amplification of picosecond pulses.

A new technique is necessary to amplify short pulses to saturation energies while maintaining a low power level in the amplifier. We have developed such a technique using chirped pulse amplification (CPA); it is illustrated in Fig. 31.23: a short optical pulse is initially chirped and stretched, allowing it to be amplified to saturation while maintaining relatively low peak power. After amplification, an optical compressor is used to restore the original short pulse width, producing a pulse with short duration and large energy.

There are two methods for expanding and compressing the optical pulses. The first method uses the fiber-grating compression technique, as will be shown in the next section. The second method uses a grating pair, for both stretching and compressing, and will be described at the end of this article.

Generation of 0.5-TW, 1-ps Pulses

As has been previously reported, we have demonstrated the CPA technique using a fiber-grating compression system.[5,6] The original CPA system employed a Nd:YAG oscillator and silicate glass amplifiers to produce 100-mJ pulses with durations of 2 ps. Presently we are using a cw-pumped mode-locked Nd:YLF laser, which

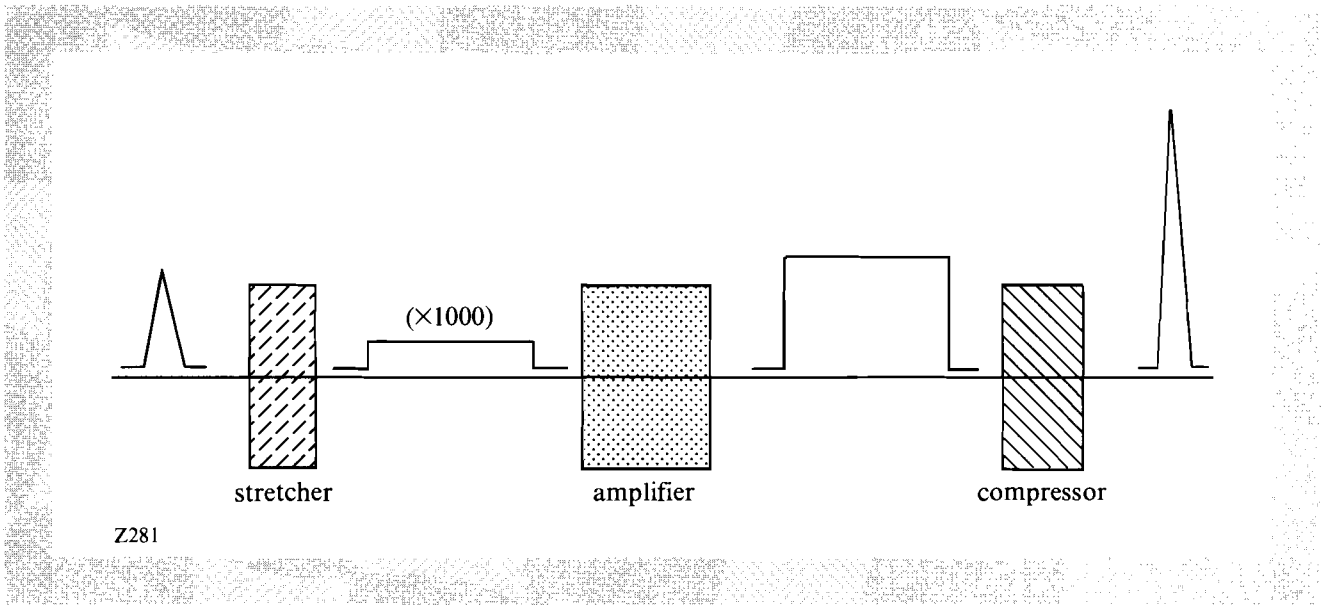

Fig. 31.23
Chirped-pulse amplification technique.

produces 55-ps pulses and therefore allows shorter compressed pulse widths.[7] Another advantage of Nd:YLF is that its wavelength matches that of phosphate Nd:glass amplifiers, which have better thermal properties than silicate glass. The current CPA system generates 0.5-TW pulses of 1-ps duration.

A schematic of the laser system is shown in Fig. 31.24. A cw-pumped mode-locked Nd:YLF oscillator generates a 100-MHz train of 55-ps pulses at a wavelength of 1.053 μm. The pulses are coupled into a 9-μm core, 1.3-km single-mode optical fiber. Due to both self-phase modulation and group velocity dispersion (GVD), the pulses are linearly chirped to 300 ps across a 3.5-nm bandwidth.[8] At this point, the pulses can be compressed to 1 ps using a double-pass grating compressor, as shown in Fig. 31.25.[9] With the CPA technique, the chirped (300-ps) pulses are first amplified and then compressed. By using this technique, 300 times more energy can be extracted than by directly amplifying a compressed 1-ps pulse.

The chirped pulses are amplified in phosphate Nd:glass (Kigre Q98), whose fluorescence peak at 1.053 μm matches the oscillator wavelength. Its bandwidth (21 nm) allows for amplification of 100-fs pulses. Joule energies are achieved using three flash-lamp-pumped amplifiers. A schematic of the amplification stage is shown in Fig. 31.26. The first stage is a regenerative amplifier operating at 5 Hz. The pulse undertakes ~100 round trips to reach saturation in a linear cavity containing a 7-mm-diameter rod before being switched out. At this stage, the pulse energy has been increased by more than six orders of magnitude, from 1 nJ to 2 mJ. After upcollimation, the pulse is amplified to 100 mJ in a four-pass, 9-mm-diameter amplifier. The pulse is then upcollimated a second time and spatially filtered before being amplified in the third stage. This final stage consists of a 16-mm-diameter rod used in single pass, which brings the energy level of the pulse to over 1 J.

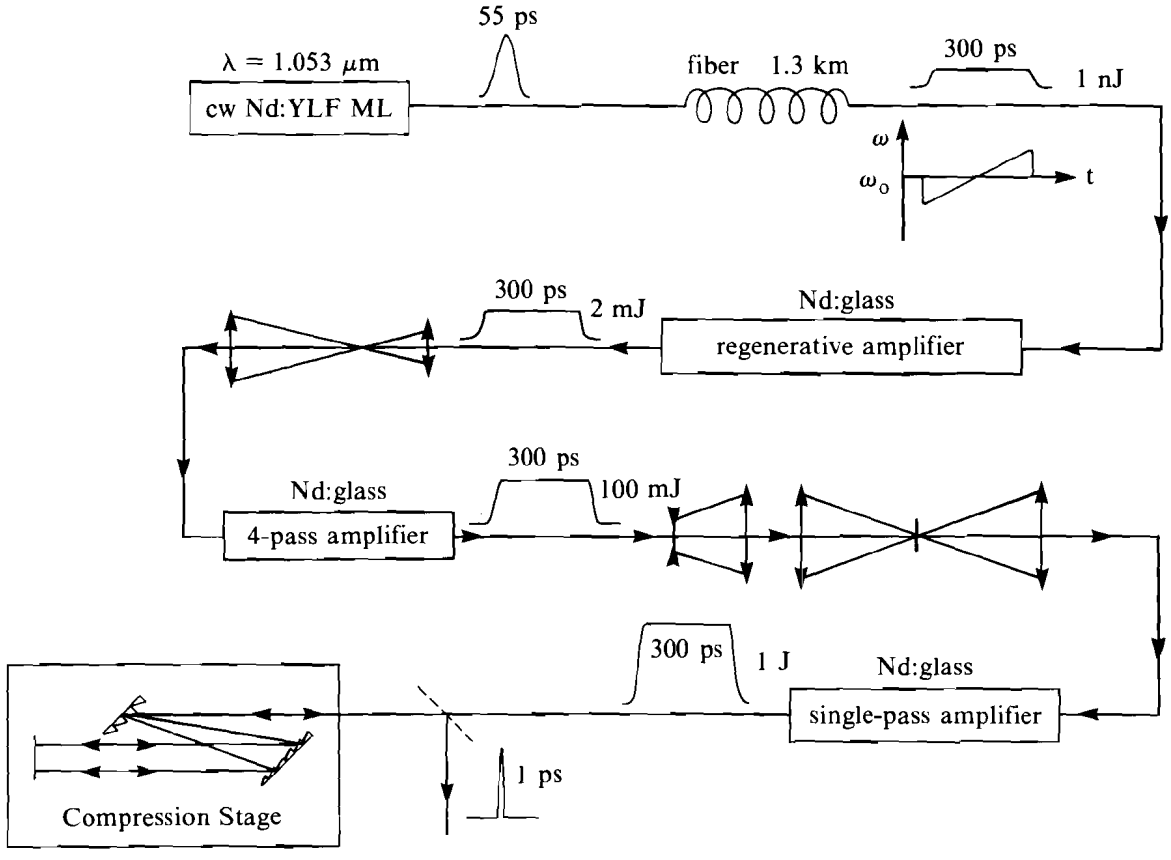

Fig. 31.24
Diagram of the current laser system.

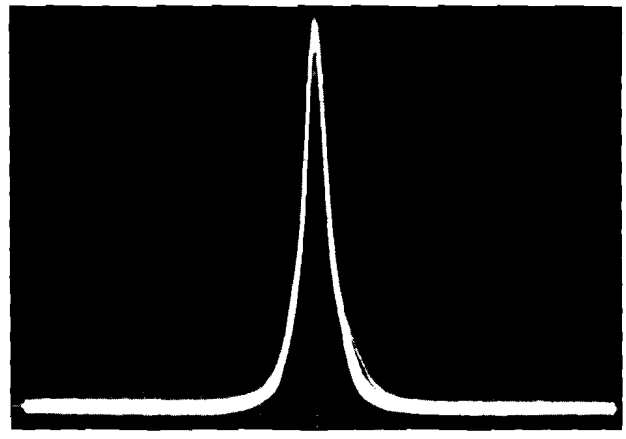

Fig. 31.25
Autocorrelation trace of the compressed Nd:YLF, showing a pulse width of 1 ps assuming a Gaussian profile.

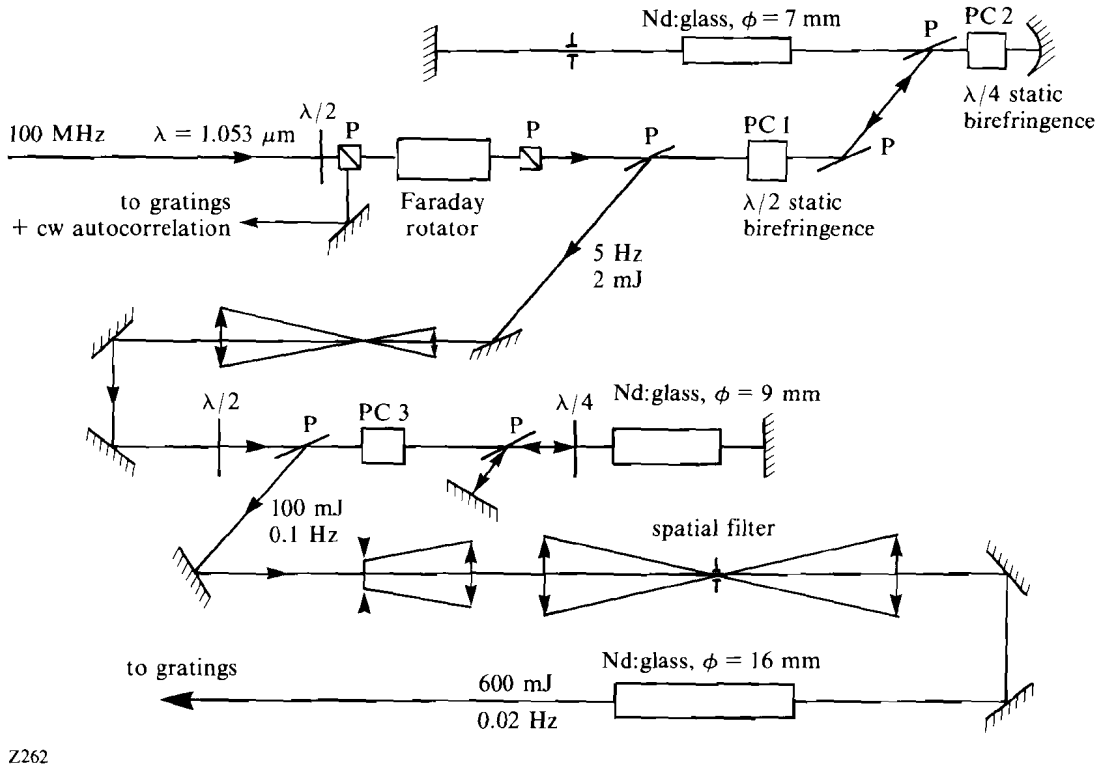

Fig. 31.26
Schematic of the amplification stage.

The compression stage consists of two gold-coated holographic gratings with 1700 ℓ/mm that are used in near-Littrow configuration. The single-pass efficiency of the compression stage is 90% for *p*-polarized light. In order to operate below the damage threshold of the gratings ($\sim$ 100 mJ/cm^2), a conservative value of 20 mJ/cm^2 on the grating has been adopted. Therefore, only 500 mJ can be incident on our current gratings, which have dimensions of 7 $\times$ 7 cm^2. To have maximum pulse energy, we use the compressor in a single-pass configuration.

The pulse-width measurement was carried out using a single-shot autocorrelator based on noncollinear second-harmonic generation.[10] A schematic of the apparatus is given in Fig. 31.27, and the autocorrelation trace is shown in Fig. 31.28. Assuming gaussian profile, the pulse width is 1-ps FWHM. This yields a 0.5-TW pulse at output of the system, the repetition rate of which is limited by the power conditioning of our 16-mm amplifier to one shot every 50 s. Slab amplifiers could be operated faster than 1 Hz.

We have recently measured the beam divergence of the compressed pulse at the 1-mJ level (with only the first amplifier), and at 250 mJ (with the three amplifiers), using a long focal lens (5 m) and a detector array. Results show the 1-mJ, 1-ps pulse to be 1.4 times diffraction limited, making possible intensities greater than 10^{16} W/cm^2 with an

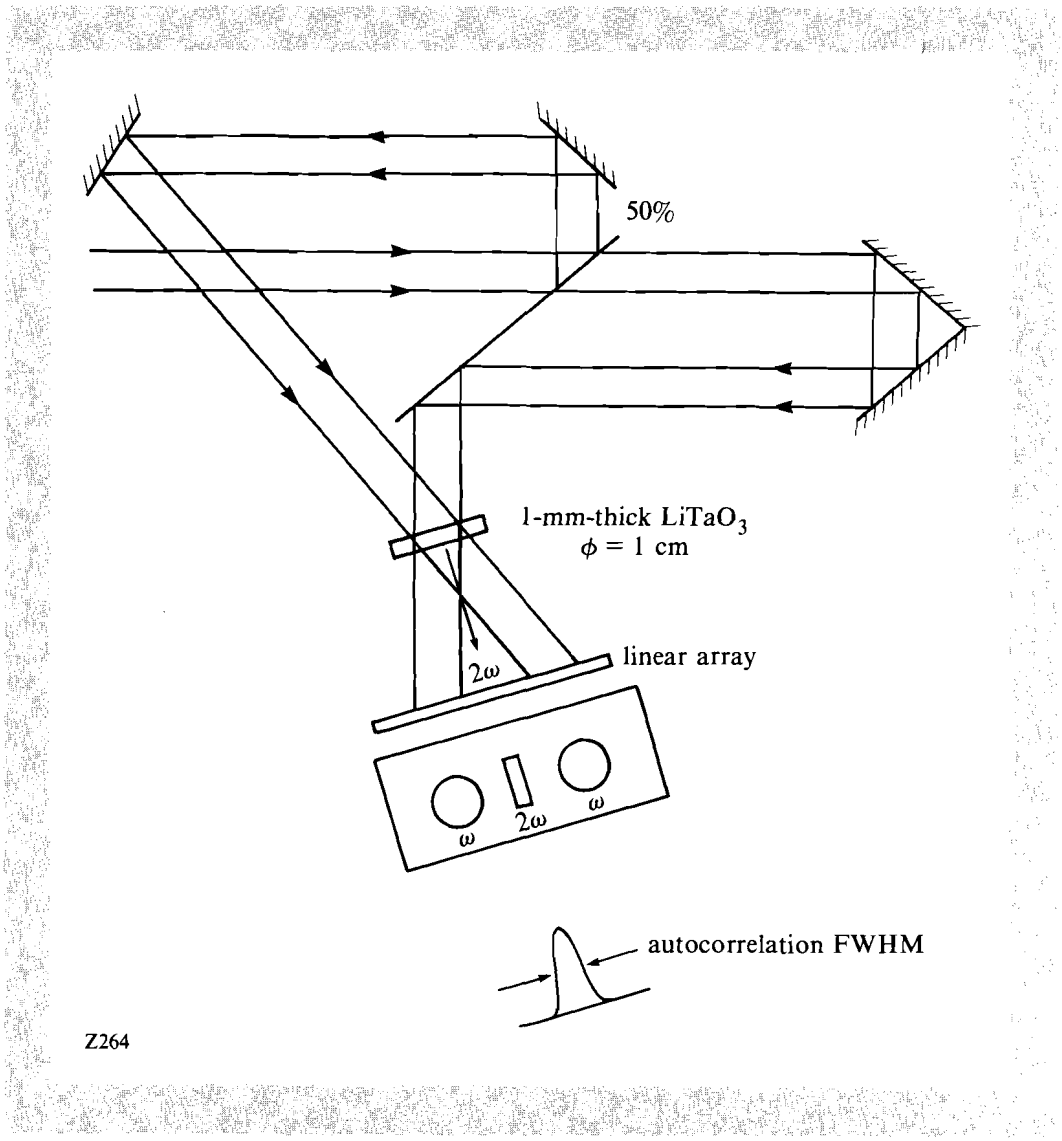

Fig. 31.27
Single-shot autocorrelator.

f/1 lens. Measurements done for the 250-mJ pulses show a 2.2 times diffraction-limited focal spot. This will yield, when focused with an *f*/1 lens, intensities greater than 10^{18} W/cm^2. We attribute the discrepancy between the two focal-spot measurements to a defocusing aberration induced by the thermal lensing of the 16-mm amplifier, most of which could be compensated by proper relocation of the target plane.

To our knowledge, this represents the highest brightness ever achieved. The system needed to generate this performance is remarkably compact: the amplification system that brings the pulse to the joule level stands easily on a 4′ × 8′ table. Furthermore, it has yet to be optimized, and a longer stretched pulse (1 ns) in conjunction with larger gratings will allow us to extract 3 to 4 J out of the last amplifier, while compression optimization will lead to a final pulse of approximately 500 fs. These modifications should produce a peak power of ~6 TW without degrading the focusability, making possible intensities greater than 10^{19} W/cm^2.

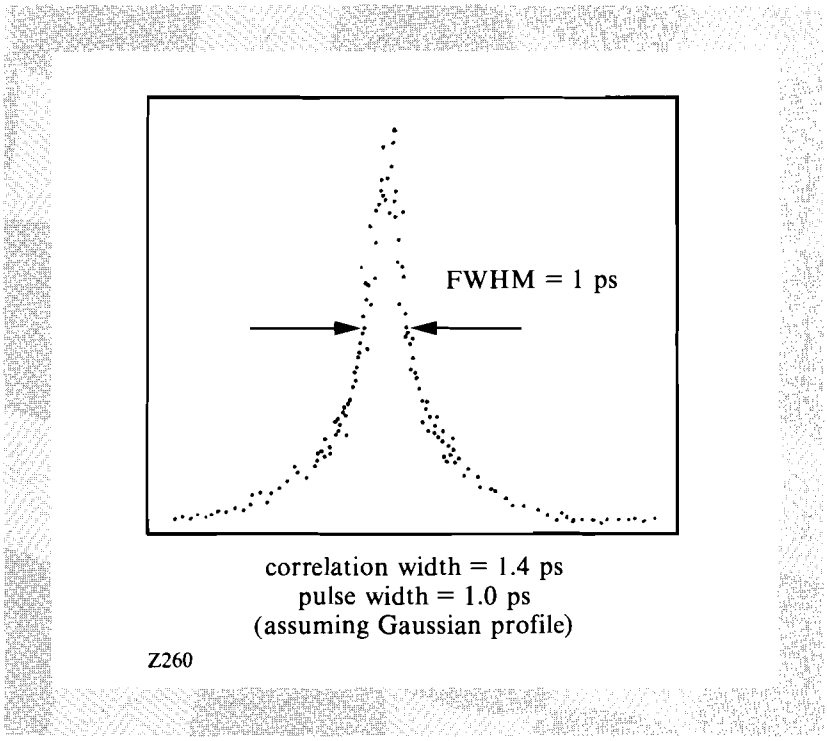

Fig. 31.28
Autocorrelation trace of the 500-mJ pulse, showing a pulse width of 1 ps assuming a Gaussian profile.

Toward Higher Peak Power: the Expansion-Compression Approach

In order to fully exploit the potential of CPA, it is desirable to have the largest ratio between the chirped and compressed pulses. The use of a fiber-grating system for the chirping and subsequent compression imposes certain constraints and limitations on the achievable ratio of the chirped-pulse duration to the compressed-pulse duration r. Single-stage compression of cw mode-locked YAG or YLF is limited to approximately an r of 300. This limitation stems from the nonlinear relationship of the group delay versus wavelength for a grating pair. The delay between spectral components arising from dispersion within the fiber can only be compensated by a grating pair to the first order.

The group time delay $\tau = d\rho/d\omega$ from a grating pair in double pass can be written to the second order as[11]

$$\tau(\lambda_o+\Delta\lambda) = \tau_o+2\frac{\lambda_o}{c} L\frac{m^2}{a^2\cos^3\theta}\Delta\lambda + \frac{3L\,m^2}{c\,a^2\,\cos^3\theta}\left(1+\frac{\lambda_o m\,\sin\theta}{a\,\cos^2\theta}\right)(\Delta\lambda)^2 = \tau_o+\tau_1+\tau_2\ , \tag{2}$$

where $\lambda = \lambda_o + \Delta\lambda$ is the wavelength, λ_o the central wavelength of the pulse, c the speed of light, L the distance between the planes containing the gratings, m the diffraction order, a the line spacing, and θ the diffracted angle.

A linearly chirped pulse can then be compressed by adjusting the grating parameters to cancel the first-order term, leaving the pulse with a residual chirp described by τ_2. We have simulated the autocorrelation and temporal profile of such a compressed pulse for parameters appropriate to our system. Figure 31.29 demonstrates the effect of τ_2 as the chirped-pulse duration increases, while bandwidth remains constant. The grating spacing has been chosen to cancel τ_1. Increased side lobes are seen in the autocorrelation function, while the FWHM is only marginally affected. The temporal profile shows a more severe effect, where a quadratic delay induces a beating between wavelengths symmetrically displaced with respect to the central wavelength. This leads to a strongly modulated temporal profile (Fig. 31.30). Measurements done with a cw mode-locked Nd:YAG coupled into a 2.4-km fiber show the importance of the quadratic term: when using the entire 4-nm spectrum, the autocorrelation indicates a pulse width of 1.2-ps FWHM, but it exhibits a large pedestal (Fig. 31.31). Using an 0.8-nm interference filter—leaving all other parameters identical—results in a very clean 2-ps pulse (Fig. 31.32). Shorter compressed pulses could also be obtained by using a two-stage compression system. This would not help in bringing about higher peak powers because the chirped pulse the amplifier sees will also be substantially shorter. It is also possible to obtain longer chirped pulses by using a longer optical fiber. This is not a viable alternative, however, because the longer fiber affects the linearity of the chirped pulse and will negatively affect the quality of the compressed pulse.

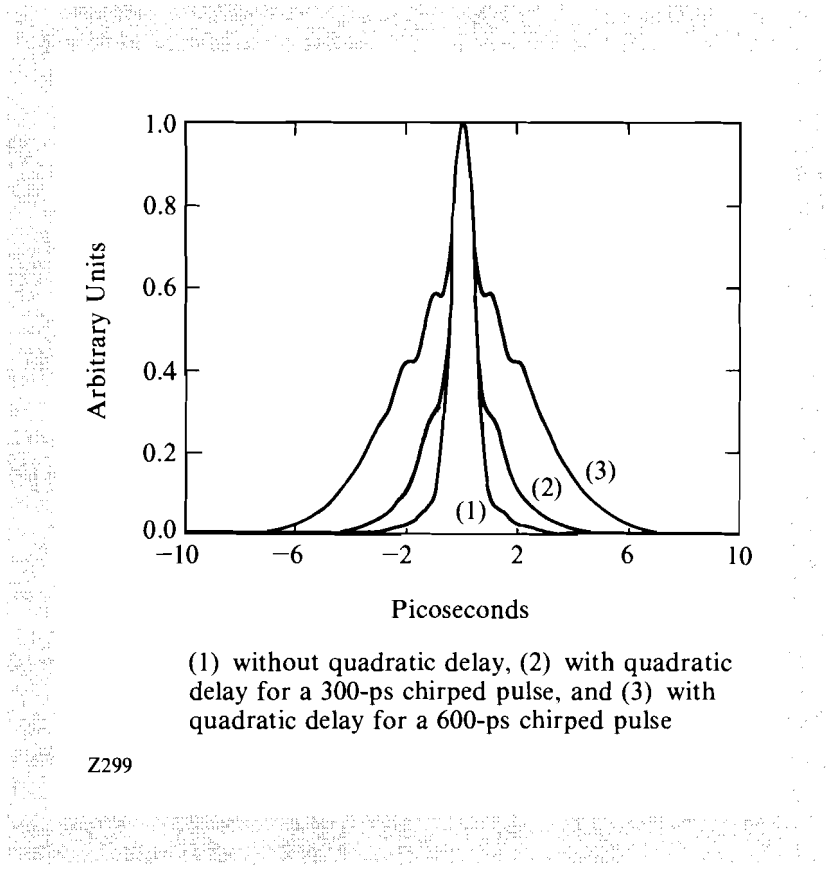

(1) without quadratic delay, (2) with quadratic delay for a 300-ps chirped pulse, and (3) with quadratic delay for a 600-ps chirped pulse

Z299

Fig. 31.29
Autocorrelation of compressed/chirped pulses.

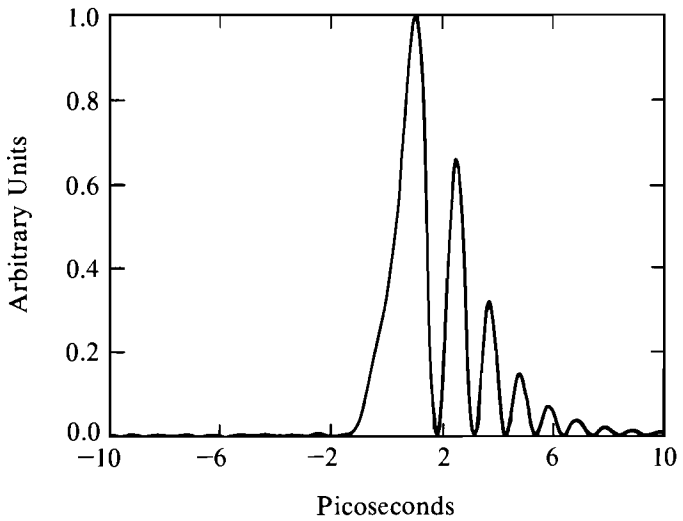

Z300

Fig. 31.30
Temporal profile resulting from the compression of a 600-ps chirped pulse.

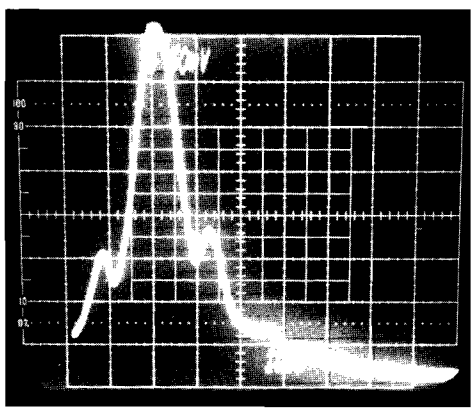

40-Å spectrum
2.4-km-long fiber
FWHM = 1.2 ps

Z297

Fig. 31.31
Autocorrelation trace of a 40-Å-bandwidth compressed pulse.

Both simulation and experiments clearly show the limitation of fiber-grating compression for the CPA technique that arises from the mismatch of the dispersive properties of the fiber and the grating pair. The same problem is encountered in the compression of femtosecond pulses. Brito-Cruz was able to overcome this and generate 6-fs pulses by using a combination grating and prism compressor.[12] This solution is not applicable here; prisms are not dispersive enough to yield reasonable physical dimensions in the picosecond domain. However, it is possible to use gratings to do both the compression and expansion.

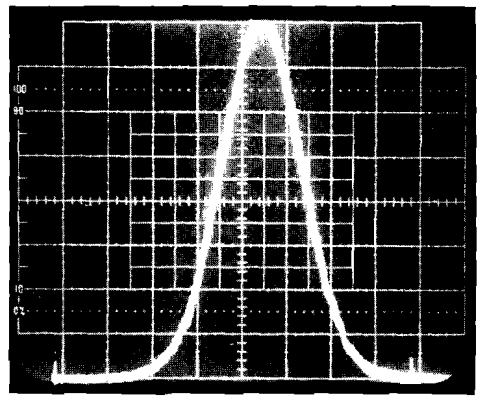

Fig. 31.32
Autocorrelation trace of a filtered 8-Å-bandwidth compressed pulse.

The source used for these experiments was a synchronously pumped, colliding-pulse, mode-locked antiresonant ring dye laser,[13] which delivers 80-fs pulses at a 100-MHz repetition rate. The bandwidth of the laser was 48 Å (FWHM), centered at 617 nm.

The experimental arrangement for both stretching and recompressing the pulse is shown in Fig. 31.33. Two 1700-ℓ/mm reflection gratings are arranged in an antiparallel configuration with a separation of 128 cm, with the laser beam incident about 10° away from Littrow. Between the grating pair, and nearly symmetric with respect to the gratings, are two 500-mm-focal-length lenses separated by 1 m to form a telescope with unit magnification. A corner reflector is used to double-pass through the system, both for compactness and to keep a circular beam profile.

As shown by Martinez,[14] the telescope inverts the angular dispersion, resulting in a net-positive group-velocity dispersion provided that the gratings lie inside the focal planes of the lenses. The effective separation contributing to the dispersion (single pass) is then given by the sum of the distances from each grating to the adjacent focal plane—72 cm for the above arrangement.

The input pulse to the system was measured by the standard second-harmonic-generation autocorrelation method to be 83-fs long (assuming a sech^2 pulse shape). Figure 31.34 shows a synchroscan streak-camera image of the pulse after propagation through the first grating pair. The pulse duration is measured to be 85-ps long, more than 1000 times its original length. As expected from a linearly dispersive system, the pulse shape still resembles a sech^2 and does not square off, as in the standard fiber-grating compression technique.

Like a pulse chirped by self-phase modulation, the stretched pulse now has a positive frequency sweep and can be compressed by another

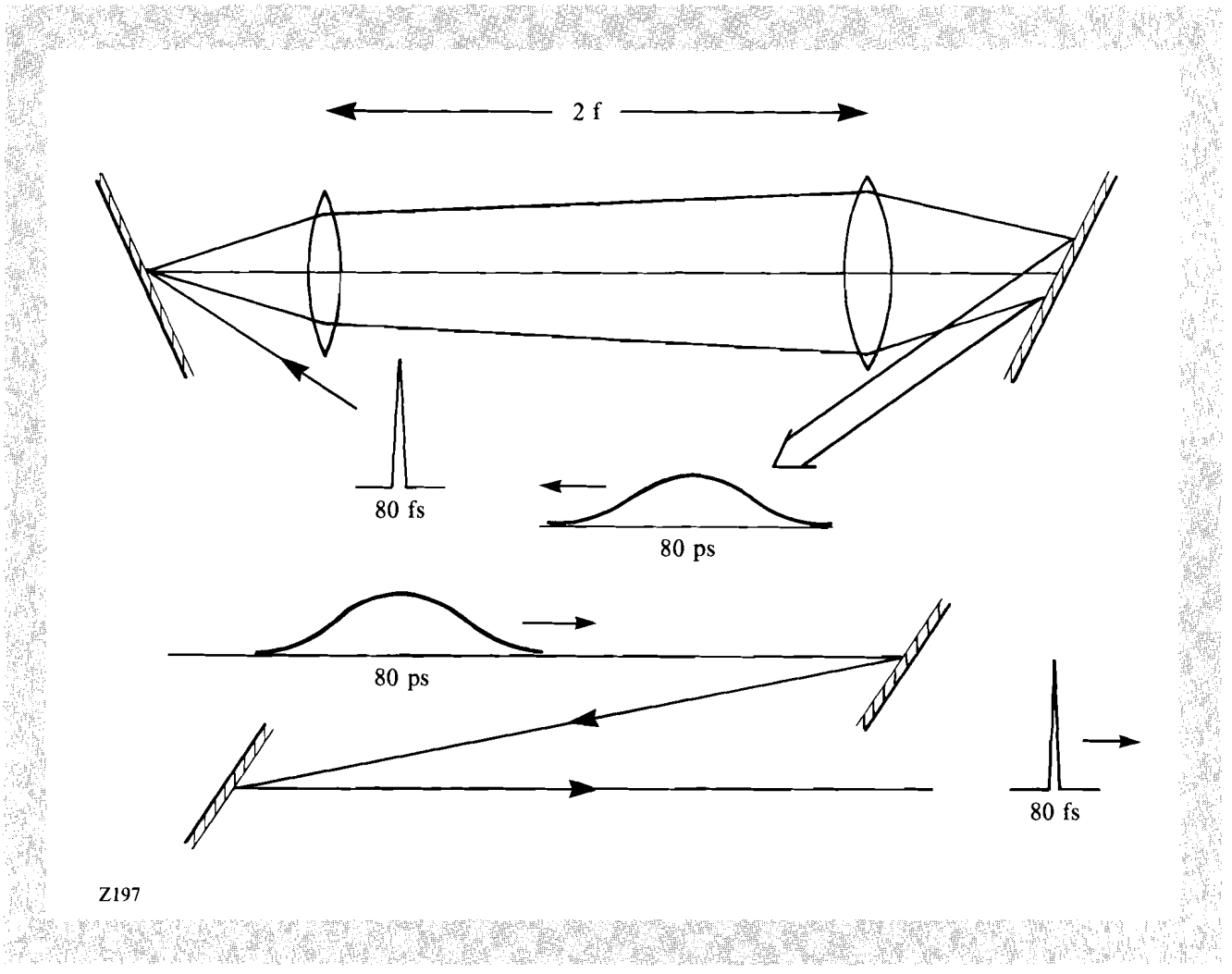

Fig. 31.33
Expansion-compression setup.

pair of gratings. Because the initial chirp was produced by a pair of gratings, it becomes possible to completely compensate for the positive chirp and restore the pulse to its original duration. A pulse that has been linearly chirped in a fiber sees a limitation, due to the fact that the variation of group delay with frequency for a grating pair is not exactly linear. For a linearly chirped 85-ps pulse with ~50-Å bandwidth, this residual nonlinearity would limit the compression to ~1 ps. This limitation has been observed in compression of both picosecond and femtosecond pulses.

A second pair of gratings (identical to the first), arranged parallel in a near-Littrow, double-pass configuration separated by 66 cm, is used to compress the pulse back to its original duration. The separation of the second pair of gratings is slightly less than the effective separation of the first pair because of the different angle of incidence of the beam with respect to the grating normal. This results in a different value of the dispersion for each grating pair. After exiting the system, the pulse duration was measured by performing a background-free cross correlation of the output of the system, with a portion of the original pulse in a 200-μm-thick $LiIO_3$ crystal. Figure 31.35 shows a

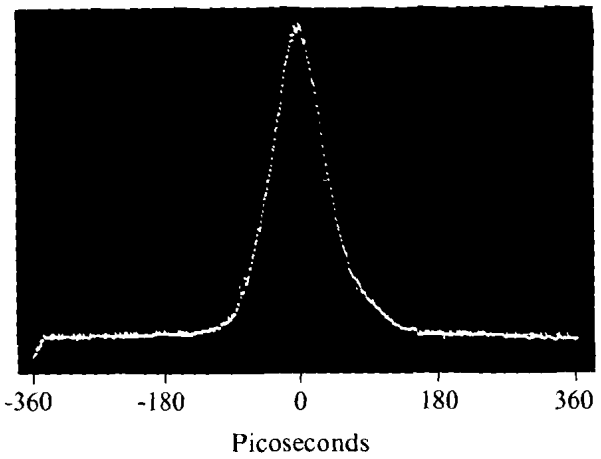

Fig. 31.34
Streak-camera image of pulse after the first grating pair. Pulsewidth (FWHM) = 85 ps. Full sweep = 720 ps.

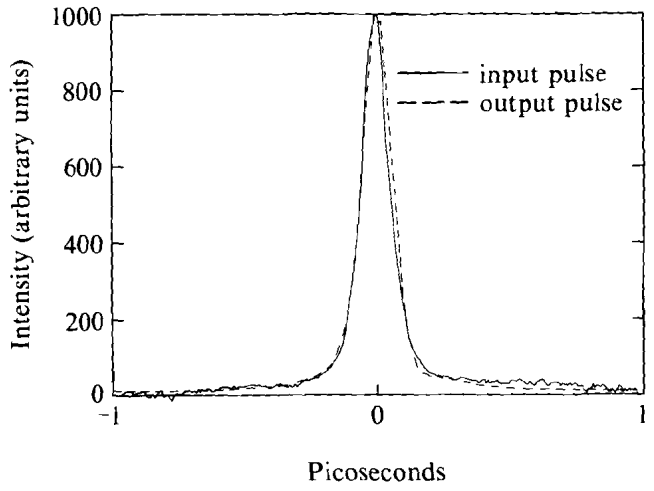

Fig. 31.35
Overlapped autocorrelation trace of the input and output pulses from the expansion-compression stage.

comparison of an autocorrelation of the input pulse and a cross correlation of the input with the output pulse. The measured correlation widths (FWHM) agree to within 10%, showing pulse durations of ~83 fs and 91 fs respectively (again, assuming a sech^2 pulse shape for deconvolution). The difference is attributed to long-term fluctuations in the dye-laser pulse width during the course of the experiment. The traces show a compression factor of ~1000 times, from 85 ps to the 85-fs to 90-fs level.

By using this technique, we are able to completely decouple the duration of the short compressed pulse from the duration of the long

chirped pulse. This makes it feasible to consider double-stage compression of the YLF oscillator to generate pulses of the order of 100 fs (a dye oscillator at the proper wavelength would also be suitable). Subsequent expansion to ~ 500 ps prior to amplification would allow us to take full advantage of the bandwidth of the Nd:glass medium. Amplification to the joule level followed by compression will lead to pulses of ~ 1 J/100 fs = 10 TW peak power with our current amplification system.

In conclusion, chirped-pulse amplification has been used to produce single picosecond pulses at the terawatt level. The beam divergence is 2.2 times the diffraction limit, making the brightness of this source greater than 10^{18} W/cm^2 · $\Delta\Omega$, the highest brightness ever reported. Presently, the technique of CPA uses a combination of fiber and grating pair. This technique is limited to a compression of only a few hundred times, due to the higher-order dispersion term in the grating pair. A better embodiment of the chirped-pulse amplification technique uses two grating pairs for pulse expansion and compression. This technique, which has already shown an expansion-compression ratio of 1000, could be improved to obtain an expansion-compression ratio greater than 5000. With the present amplifier, short pulses of a few hundred femtoseconds that were stretched to around 1 ns could be efficiently amplified to a few joules before being recompressed to their initial value, to produce pulses at the 10-TW level with essentially the same-size amplifier system. Even more exciting is the fact that the CPA technique can be used with a very large Nd:glass amplifier, such as the glass development laser at LLE. Approximately 1 kJ can be extracted from this system with a 1-ns pulse. These pulses could then be recompressed to the subpicosecond level, producing pulses well in the petawatt regime. When focused to a few times the diffraction limit, a power density well over 10^{20} W/cm^2 could be achieved.

ACKNOWLEDGMENT

This work was supported by the United States Air Force Office of Scientific Research under contract F49620-87-C-0016 to the Ultrafast Optical Electronics Center at the Laboratory for Laser Energetics of the University of Rochester and by the Laser Fusion Feasibility Project at the Laboratory for Laser Energetics, which has the following sponsors: Empire State Electric Energy Research Corporation, General Electric Company, New York State Energy Research and Development Authority, Ontario Hydro, and the University of Rochester. Such support does not imply endorsement of the content by any of the above parties.

We thank the Laboratoire d'Optique Appliquée, E.N.S.T.A., Palaiseau, France, for the loan of the 16-mm amplifier.

REFERENCES

1. W. Koechner, *Solid-State Laser Engineering* (Springer-Verlag, New York, 1976), p. 581.
2. A. P. Schwarzenbach *et al.*, *Opt. Lett.* **11**, 499 (1986).
3. L. G. Deshazer, "Advances in Tunable Solid-State Lasers," *Laser Focus/E-O Technol.* **23**, 54 (1987).
4. C. E. Cook, *Proc. IRE* **48**, 310–316 (1960).
5. D. Strickland and G. Mourou, *Opt. Commun.* **56**, 219 (1985).

6. D. Strickland, P. Maine, M. Bouvier, S. Williamson, and G. Mourou, in *Ultrafast Phenomena V*, edited by G. R. Fleming and A. E. Sigman, (Springer-Verlag, New York, 1986), pp. 38–42 .

7. P. Bado, M. Bouvier, and J. S. Coe, *Opt. Lett.* **12**, 319 (1987).

8. H. Nakatsuka and D. Grischkowsky, *Opt. Lett.* **6**, 13 (1981).

9. J. Desbois, P. Tournois, and F. Gires, *IEEE J. Quantum Electron.* **QE-9**, 213 (1973).

10. J. Janszky, G. Corradi, and R. N. Gyuzalian, *Opt. Commun.* **23**, 293 (1977).

11. J. D. McMullen, *Appl. Opt.* **18**, 737 (1979).

12. C. H. Brito-Cruz, R. L. Fork, and C. V. Shank, "Compression of Optical Pulses to 6 fs Using Cubic Phase Distortion Compensation," paper MD1, CLEO (1987).

13. T. Norris, T. Sizer II, and G. Mourou, *J. Opt. Soc. Am. B* **2**, 613 (1985).

14. O. E. Martinez, *IEEE J. Quantum Electron.* **QE-23**, 59 (1987).

Section 3
NATIONAL LASER USERS FACILITY NEWS

National Laser Users Facility (NLUF) activity during the third quarter of FY87 supported the experiments from three users.

Dr. David Bradley from the Lawrence Berkeley Laboratory has been collecting data from CH targets having Al and Mg tracer layers with the SPEAXS instrument, in support of **Dr. Burton Henke**'s NLUF experiment. The targets were designed to measure the progress of the ablation front as it moves through the layers of CH and metal. There is a marked difference between the targets with a CH outer layer and targets with a metal outer layer. The SPEAXS instrument was used to measure x rays when emitted by the Al and Mg layers.

Dr. J. Seely from the Naval Research Laboratory (NRL) collected XUV spectra from targets with a Nd layer with the NRL 3-m grazing-incidence spectrograph. These shots completed the neon-like ionization series study for high-Z ions.

Drs. T. R. Fisher, **D. Kohler**, and **P. Filbert** from the Lockheed Palo Alto Research Laboratory and **Dr. G. Dahlbacka** from Plasma Research Corporation obtained XUV spectra from a laser-heated argon gas jet. The argon was released into the OMEGA target chamber through a Mach 8 supersonic nozzle. This experiment is designed to study the ionization-state time evolution of a uniformly heated plasma. The XUV spectra show that eight UV beams of OMEGA heated the argon plasma to about 40 eV to 60 eV. More work is needed if the higher ionization states are to be studied.

For more information about proposal guidelines and the resources available at the users facility, please contact

Manager
National Laser Users Facility
Laboratory for Laser Energetics
University of Rochester
250 East River Road
Rochester, New York 14623-1299
(716) 275-2074

ACKNOWLEDGMENT

This work was supported by the U.S. Department of Energy Office of Inertial Fusion under agreement No. DE-FC08-85DP40200.

Section 4
LASER SYSTEM REPORT

4.A GDL Facility Report

GDL was active the entire period as a target interaction facility. The various experiments supported by GDL included x-ray conversion tests; preliminary studies for x-ray laser experiments; a number of shots to evaluate the benevolent smoothing effect of irradiating targets with laser beams that pass through a background inert gas, such as helium; and several ALPHA backlight experiments, where the GDL beam was transported to the OMEGA chamber.

A summary of GDL operations for this quarter follows:

Target Shots (BETA)	213
ALPHA Shots	5
Pointing Shots	83
Beamline Test Shots	99
TOTAL	400

4.B OMEGA Facility Report

The OMEGA laser system spent the entire period serving as a target irradiation facility for various experimental campaigns. On-target energy from the system remained at approximately 1.5 kJ. The beam-to-beam energy imbalance was reduced as low as 3%. The energy and

uniformity levels were sufficient to drive several targets to densities exceeding 50 times liquid DT density. By the end of the period, the first shots were being taken on targets frozen to solid DT temperatures. This was made possible by the installation of the cryogenic target system designed and fabricated by KMS Fusion.

Throughout April, the laser system was put to extensive service in support of the high-density campaign. The ALPHA beam, i.e., the GDL output transported to the OMEGA chamber, was put in service for several x-ray backlight experiments. Time-resolved ionization studies and secondary neutron activation experiments were also conducted during this period.

During May the laser was used for NLUF experiments. Eight of the OMEGA beams were focused inside a "jet" of inert gas injected into the chamber at a velocity of Mach 2 to study x rays. Late in May, the target chamber left service for the installation of the cryogenic target positioner. While not in service as a target facility, the laser was used to measure driver-line phase, with the objective of improving overall system uniformity. In addition, the pinholes were tested in selected spatial filters, and damage tests were performed on liquid-crystal polarizers. The polarizers withstood IR fluences required to produce 85 J of UV per beam. This would lead to system UV energies in excess of 2 kJ.

The last part of the period was spent activating the cryogenic target positioner. Many members of the operations group were involved in support of the installation and activation. Throughout the activation period, OMEGA provided shots on demand for checkout and for initial implosion experiments using cryogenic targets.

A summary of OMEGA operations for this quarter follows:

Target Shots	174
Beamline Test Shots	59
Driver-Line Shots	86
TOTAL	319

ACKNOWLEDGMENT

This work was supported by the U.S. Department of Energy Office of Inertial Fusion under agreement No. DE-FC08-85DP40200, and by the Laser Fusion Feasibility Project at the Laboratory for Laser Energetics, which has the following sponsors: Empire State Electric Energy Research Corporation, General Electric Company, New York State Energy Research and Development Authority, Ontario Hydro, and the University of Rochester. Such support does not imply endorsement of the content by any of the above parties.

PUBLICATIONS AND CONFERENCE PRESENTATIONS

Publications

H. L. Helfer and R. L. McCrory, "Some Properties of a Polarized OCP," in *Strongly Coupled Plasma Physics*, edited by F. J. Rogers and H. E. DeWitt (Plenum, NY, 1987), pp. 41–44.

R. L. McCrory, "Industry and University Roles in Fusion Development – Panel Discussion," *J. Fusion Energy* **6**, 184–187 (1987).

D. R. Dykaar, R. Sobolewski, T. Y. Hsiang, and G. A. Mourou, "Response of a Josephson Junction to a Stepped Voltage Pulse," *IEEE Trans. Magn.* **MAG-23**, 767-770 (1987).

S. H. Batha and C. J. McKinstrie, "Temporal Energy Cascading in the Beat-Wave Accelerator," *IEEE Trans. Plasma Sci.* **PS-15**, 131–133 (1987).

C. M. Brown, J. O. Ekberg, U. Feldman, J. F. Seely, M. C. Richardson, F. J. Marshall, and W. E. Behring, "Transitions in Lithiumlike Cu^{26+} and Berylliumlike Cu^{25+} of Interest for X-Ray Laser Research," *J. Opt. Soc. Am. B* **4**, 533–538 (1987).

R. A. Lawton and K. Meyer, "Waveform Standards for Electro-Optics: A Pulse Duration Comparison," *IEEE Trans. Microwave Theory Tech.* **MTT-35**, 450–453 (1987).

P. Bado, M. Bouvier, and J. S. Coe, "Nd:YLF Mode-Locked Oscillator and Regenerative Amplifier," *Opt. Lett.* **12**, 319–321 (1987).

M. Pessot, P. Maine, and G. Mourou, "1000 Times Expansion/Compression of Optical Pulses for Chirped Pulse

Amplification," *Opt. Commun.* **62**, 419–421 (1987).

J. S. Wark, R. R. Whitlock, A. Hauer, J. E. Swain, and P. J. Solone, "Shock Launching in Silicon Studied with Use of Pulsed X-Ray Diffraction," *Phys. Rev. B* **35**, 9391–9394 (1987).

M. A. Loudiana, J. T. Dickinson, A. Schmid, and E. J. Ashley, "Electron Enhanced Sorption of Flourine by Silver Surfaces," *Appl. Surf. Sci.* **28**, 311–322 (1987).

Forthcoming Publications

The following papers are to be published in the *Proceedings of the 17th Annual Boulder Damage Symposium*, Boulder, CO, October 1985:

K. A. Cerqua, S. D. Jacobs, B. L. McIntyre, and W. Zhong, "Ion Exchange Strengthening of Nd-Doped Phosphate Laser Glass."

B. Liao, D. J. Smith, and B. L. McIntyre, "The Development of Nodular Defects in Optical Coatings."

D. J. Smith, B. Krakauer, C. J. Hayden, A. W. Schmid, and M. J. Guardalben, "Yttrium-Oxide-Based Anti-Reflection Coating for High Power Lasers at 351 nm."

B. Yaakobi, "X-Ray Diagnostic Methods for Laser-Imploded Targets" and "Thermal Transport, Mass Ablation, and Preheat in Laser-Target Experiments," to be published in the *Proceedings of the Spring College on Radiation in Plasmas*, Trieste, Italy, June 1985 (World Scientific Publishing Co.).

G. Mourou, "Picosecond Electro-Optic Sampling," to be published in the *Proceedings of the High Speed Electronics Conference*, Stockholm, Sweden, August 1986.

S. M. Gracewski and R. Q. Gram, "Analysis of Forces on ICF Targets During Ablation Layer Coating," to be published in the *Journal of Vacuum Science and Technology*.

K. A. Cerqua, S. D. Jacobs, and A. Lindquist, "Ion-Exchange Strengthened Phosphate Laser Glass: Development and Applications," to be published in the *Journal of Non-Crystalline Solids*.

K. A. Cerqua, A. Lindquist, S. D. Jacobs, and J. Lambropoulos, "Strengthened Glass for High-Average-Power Laser Applications," to be published in the *Proceedings of SPIE's O-E LASE 1987 Conference*.

H. Kim and M. Wittman, "X-Ray Microscopy of Inertial Fusion Targets Using a Laser-Produced Plasma as an X-Ray Source," to be published in the *Journal of Vacuum Science and Technology*.

H. E. Elsayed-Ali and G. A. Mourou, "Phase Transitions in the Picosecond Time Domain," to be published in the *Proceedings of the 1986 Materials Research Society Meeting*, Boston, MA, December 1986.

W. R. Donaldson, "High-Speed, High-Repetition-Rate, High-Voltage Photoconductive Switching," to be published in the *Proceedings of the 2nd Topical Meeting on Picosecond Electronics and Optoelectronics*, Lake Tahoe, NV, January 1987.

G. Mourou, K. Meyer, J. Whitaker, M. Pessot, R. Grondin, and C. Caruso, "Ultrafast Optics Applied to Modern Device Research," to be published in the *Proceedings of the 2nd Topical Meeting on Picosecond Electronics and Optoelectronics*, Lake Tahoe, NV, January 1987.

R. W. Short, W. Seka, and R. Bahr, "Stimulated Raman Scattering in Self-Focused Light Filaments in Laser-Produced Plasmas," to be published in *Physics of Fluids*.

J. Delettrez, R. Epstein, M. C. Richardson, P. A. Jaanimagi, and B. L. Henke, "Effect of Laser Ilumination Nonuniformity on the Analysis of Time-Resolved X-Ray Measurements in UV Spherical Transport Experiments," to be published in *Physical Review A*.

R. L. McCrory and J. M. Soures, "Inertially Confined Fusion," to be published in *Applications of Laser Plasmas,* Chapter 7.

K. A. Cerqua, J. Hayden, and W. C. LaCourse, "Stress Measurements in SOL-GEL Films," to be published in the *Journal of Non-Crystalline Solids*.

J. F. Whitaker, R. Sobolewski, D. R. Dykaar, T. Y. Hsiang, and G. A. Mourour, "Propagation Model for Ultrafast Signals on Superconducting Dispersive Striplines," to be published in a special issue of *IEEE Transactions on Microwave Theory and Techniques.*

T. Jackson, J. Nees, R. Vallee, and G. Mourou, "A Novel Method for Ultrahigh Frequency Electro-Optic Time-Domain Reflectometry," to be published in *Electronics Letters.*

T. Y. Hsiang, J. F. Whitaker, R. Sobolewski, D. R. Dykaar, and G. A. Mourou, "Propagation Characteristics of Picosecond Electrical Transients on Coplanar Striplines," to be published in *Applied Physics Letters.*

J. C. Lee, S. D. Jacobs, and A. Schmid, "Retro-Self-Focusing and Pinholing Effect in a Cholesteric Liquid Crystal," to be published in *Molecular Crystals and Liquid Crystals.*

Conference Presentations

A. Simon and R. W. Short, "Enhanced Noise and Raman Scattering in Plasma," presented at the 1987 International Conference on Plasma Physics, Kiev, USSR, April 1987 (invited paper).

G. A. Mourou, "Generation and Application of Femtosecond Optical Pulses," presented at Electo Optics/Laser '87, Tokyo, Japan, April 1987.

B. Yaakobi, "X-Ray Laser and Gamma Ray Laser Studies at the Laboratory for Laser Energetics," presented at the American Physical

Society, Washington, D. C., April 1987 (invited paper).

The following presentations were made at CLEO '87 Conference, Baltimore, MD, 27 April–1 May 1987:

T. Kessler, S. Skupsky, W. Seka, L. Feinberg, S. Jacobs, K. Marshall, N. Sampat, D. J. Smith, and S. Swales, "High-Power Glass Laser Phase Control."

J. H. Kelly, D. L. Smith, J. C. Lee, S. D. Jacobs, D. J. Smith, J. C. Lambropoulos, and M. J. Shoup III, "Active Mirror Geometry, Nd^{+3}:Cr^{+3}:GSGG Amplifier."

W. Donaldson, L. Kingsley, K. Meyer, and C. Bamber, "Semiconductor Contact Characterization Using Electro-Optic Sampling."

M. C. Richardson, P. Audebert, J. Delettrez, R. Epstein, P. Jaanimagi, R. Kremens, F. Marshall, P. McKenty, R. McCrory, S. Skupsky, W. Seka, J. Soures, C. Verdon, and J. Wark, "Polymer Shell Implosions."

P. Bado and J. S. Coe, "Nd:YLF: Demonstration of a cw-Pumped Actively Modelocked Oscillator-Regenerative Amplifier Source."

P. Maine, D. Strickland, M. Bouvier, and G. Mourou, "Amplification of Picosecond Pulses to the Terawatt Level by Chirped Pulse Amplification and Compression."

M. Pessot, P. Maine, and G. Mourou, "1000 Times Expansion/Compression System for Chirped Pulse Amplification," presented at IQEC '87, Baltimore, MD, 26 April–1 May 1987.

G. A. Mourou, "Electro-Optic Sampling Technique and Its Application to Components and Circuit Characterization," presented at ECS Symposium on Beam Testing, Philadelphia, PA, May 1987.

The following presentations were made at the 18th European Conference on Laser Interaction with Plasma, Prague, Czechoslovakia, May 1987:

R. L. McCrory, "Ultra-High Pressure, Direct-Drive, Ablative Compression."

W. Seka, T. J. Kessler, S. Skupsky, F. J. Marshall, P. A. Jaanimagi, M. C. Richardson, J. M. Soures, C. P. Verdon, and R. Bahr, "Uniformity of Illumination in Direct-Drive Laser Fusion."

The following presentations were made at the 17th Annual Anomalous Absorption Conference, Tahoe City, CA, May 1987:

P. Audebert, T. Boehly, D. Bradley, R. S. Craxton, R. Epstein, M. C. Richardson, D. Shvarts, and B. Yaakobi, "The Spectroscopic Study of Single and Double Ni Foils for X-Ray Laser Studies."

S. H. Batha, L. M. Goldman, W. Seka, and A. Simon, "Observations of Enhanced Thomson Scattering."

T. Boehly, P. Audebert, D. Bradley, R. S. Craxton, R. Epstein, M. C. Richardson, D. Shvarts, and B. Yaakobi, "An Experimental Study of Single and Double Foils for X-Ray Laser Media."

J. Delettrez, G. Gregory, P. Jaanimagi, T. Kessler, M. C. Richardson, and S. Skupsky, "Effects of Illumination Nonuniformities on the Interpretation of Streak Imaging of Glass Microballoon Implosions."

R. Epstein, D. Shvarts, S. Skupsky, and B. Yaakobi, "The Design and Optimization of Recombination X-Ray Lasers."

L. M. Goldman, "Effect of Mixing on Interpretation of Reaction Product Measurement of ρR."

R. W. Short and A. Simon, "Absolute Stimulated Raman Backscatter at High Laser Intensities."

A. Simon, R. W. Short, W. Seka, and L. M. Goldman, "Alternative Analysis of CO_2-Laser-Produced Plasma Waves."

A. Simon and R. W. Short, "Enhanced Thompson Scattering in Underdense Targets."

D. Shvarts, M. C. Richardson, B. Yaakobi, P. Audebert. T. Boehly, D. Bradley, R. S. Craxton, R. Epstein, R. L. McCrory, and J. M. Soures, "Studies on High-Density Plasma Waveguides for X-Ray Lasers."

D. Havazelet, D. Shvarts, and S. Skupsky, "Simulation of Thermal and Ponderomotive Self-Focusing in Long-Scale-Length Coronas."

D. K. Bradley, P. Audebert, J. Delettrez, R. Epstein, G. Gregory, B. L. Henke, P. A. Jaanimagi, M. C. Richardson, and B. Yaakobi, "Time-Resolved Specroscopy of Laser-Driven Spherical Targets."

P. A. Jaanimagi, G. G. Gregory, D. K. Bradley, J. Delettrez, F. J. Marshall, P. W. McKenty, M. C. Richardson, and C. P. Verdon, "Time-Resolved X-Ray Diagnosis of the Acceleration Phase of ICF Implosions."

F. J. Marshall, P. A. Jaanimagi, M. C. Richarson, C. Rapp, S. Morse, R. Hutchison, S. Noyes, T. Kessler, and W. Seka, "Uniformity of Direct-Drive Laser Illumination Measured by X-Ray Imaging."

M. C. Richardson, P. Audebert, D. Bradley, J. Delettrez, G. G. Gregory, P. A. Jaanimagi, R. Keck, R. Kremens, F. J. Marshall, R. L. McCrory, P. W. McKenty, J. M. Soures, and C. P. Verdon, "High-Density Direct-Drive Gas-Filled Target Implosions,"

R. S. Craxton, "The Application of Ray-Tracing Techniques to Laser-Plasma Simulations," (invited talk).

J. P. Knauer, O. Barnouin, R. Keck, J. Delettrez, and S. Letzring, "Energy Partitioning of Spherically Irradiated Targets."

D. R. Dykaar, R. Sobolweski, J. M. Chwalek, T. Y. Hsiang, and G. A. Mourou, "Electro-Optic Sampler for Characterization of Devices in Cyrogenic Environment," presented at the Cyrogenic Engineering Conference, St. Charles, IL, June 1987.

W. Donaldson, G. Mourou, L. Kingsley, and C. Bamber, "Characterization of High-Voltage Photoconductive Switches," presented at the IEEE Pulsed Power Conference, Arlington, VA, 29 June–1 July 1987.

K. A. Cerqua, "Recent Advances in Materials Research for Solid State Laser Applications," presented for the Industrial Ceramics Delegation Tour of China, 21 June–12 July 1987.

ACKNOWLEDGMENT

The work described in this volume includes current research at the Laboratory for Laser Energetics, which is supported by Empire State Electric Energy Research Corporation, General Electric Company, New York State Energy Research and Development Authority, Ontario Hydro, the University of Rochester, and the U.S. Department of Energy Office of Inertial Fusion under agreement No. DE-FC08-85DP40200.